01 Jun 2022

Development and Application of a 1D Compaction Model to Understand 65 Years of Subsidence in the San Joaquin Valley

Matthew Lees

Rosemary Knight

Ryan G. Smith
Missouri University of Science and Technology, smithryang@mst.edu

Recommended Citation

M. Lees et al., "Development and Application of a 1D Compaction Model to Understand 65 Years of Subsidence in the San Joaquin Valley," *Water Resources Research*, vol. 58, no. 6, article no. e2021WR031390, Wiley; American Geophysical Union, Jun 2022.
The definitive version is available at https://doi.org/10.1029/2021WR031390

AGU ADVANCING EARTH AND SPACE SCIENCE

Water Resources Research

RESEARCH ARTICLE
10.1029/2021WR031390

Development and Application of a 1D Compaction Model to Understand 65 Years of Subsidence in the San Joaquin Valley

Matthew Lees[1], **Rosemary Knight**[1], **and Ryan Smith**[2]

[1]Stanford University, Stanford, CA, USA, [2]Missouri University of Science and Technology, Rolla, MO, USA

Key Points:

- We integrated head and other measurements to create a 1D compaction model, simulating subsidence from 1952 to 2017 in the San Joaquin Valley
- The majority of compaction occurred in the lower aquifer, and the time scales for the residual compaction of clay ranged from 64 to 1,008 years
- In order to significantly reduce subsidence, there must be some recovery of head, not just a stabilization

Supporting Information:

Supporting Information may be found in the online version of this article.

Correspondence to:

M. Lees,
mlees@stanford.edu

Citation:

Lees, M., Knight, R., & Smith, R. (2022). Development and application of a 1D compaction model to understand 65 years of subsidence in the San Joaquin Valley. *Water Resources Research*, *58*, e2021WR031390. https://doi.org/10.1029/2021WR031390

Received 13 OCT 2021
Accepted 16 MAY 2022

Author Contributions:

Conceptualization: Matthew Lees, Rosemary Knight
Data curation: Matthew Lees
Formal analysis: Matthew Lees, Ryan Smith
Funding acquisition: Rosemary Knight
Investigation: Matthew Lees
Methodology: Matthew Lees, Rosemary Knight, Ryan Smith
Project Administration: Rosemary Knight
Resources: Rosemary Knight

Abstract High rates of land subsidence, caused by groundwater overdraft, are resulting in millions of dollars of infrastructure damage in California's San Joaquin Valley (SJV). In recent years, the use of interferometric synthetic aperture radar (InSAR) has enabled us to substantially improve our understanding of this subsidence. However, only very occasionally have the InSAR data been integrated with a physical model of subsurface compaction. Here, we have used InSAR and other data to parameterize and calibrate a 1D compaction model. We applied our model to a study area in the SJV where we had access to the necessary information on hydraulic head to develop model inputs. Our model simulated subsidence in the three aquifer system layers over the period 1952–2017, and is the first 1D compaction model in the SJV to simulate multiple aquifer system layers from the 1950s to 2017. The results from our model suggest that previous studies have significantly underestimated the time constants governing the slow, residual compaction of subsurface clays. We suggest that residual compaction of clays is a process that continues for decades-to-centuries, indicating that to significantly reduce subsidence requires some recovery of head, not just a stabilization. We also show how compaction in the lower, confined aquifer has accounted for over 90% of subsidence in the past 20 years. Although our study area is small, our findings are likely representative of the subsiding regions of the SJV, and our methodology can be applied to unconsolidated aquifer systems exhibiting subsidence worldwide.

1. Introduction

California's San Joaquin Valley (SJV) has experienced periods of land subsidence, triggered by the extraction of groundwater and subsequent compaction of subsurface clays, since the 1920s (Poland et al., 1975). The magnitude and extent of this subsidence have been vast: up to 9 m has been observed at some locations, while the footprint of subsiding regions exceeded 13,000 km^2 by the 1980s and has continued to grow since (Faunt et al., 2016; Ireland et al., 1984). The subsidence has been immensely damaging to long-range infrastructure crossing the Valley, in particular gravity-driven canals and aqueducts which have required remedial repairs costing 100s of millions of dollars (Borchers & Carpenter, 2014). This, in combination with a new wave of subsidence starting in the statewide 2012–2015 drought, led to subsidence being included in a groundbreaking piece of legislation, the Sustainable Groundwater Management Act (SGMA), which legally requires groundwater managers in California to make plans to reduce subsidence along with other negative impacts of groundwater extraction. Against this backdrop, it is a critical time for the study of subsidence in the Valley.

Subsidence in the Valley is a complex process. The large-scale hydrostratigraphy is a three-layered alluvial aquifer system: an upper aquifer, a regional confining unit known as the Corcoran Clay, and a lower aquifer. Within the upper and lower aquifers is a mix of sediments, which are commonly described as a coarser-grained background containing many clay interbeds. Sediments throughout the aquifer system will compact, leading to land subsidence, if there is a drop in hydraulic head within those sediments. Drops in hydraulic head are triggered when there is a net loss of water from the aquifer system, which primarily occurs when the largest sink—groundwater pumping—exceeds recharge, a circumstance known as overdraft. Overdraft conditions have occurred repeatedly in the SJV since the early 20th century. Importantly, the head drops do not occur simultaneously in all of the sediments. Since they are hydraulically conductive, pumping and recharge both occur in the coarser-grained sediments, and head accordingly drops first in these materials. However, the head in the Corcoran Clay and clay interbeds only responds gradually, because clay has a low hydraulic conductivity. This gradual decline in head in clay layers means they experience so-called residual compaction, a process which can continue long after the overdraft which initiated it. The compaction of clays is the primary origin of subsidence, since clay is far more compressible than the coarser-grained materials. Together, these complexities mean that the subsidence is heterogeneous in space and time, thus challenging to study.

Software: Matthew Lees
Supervision: Rosemary Knight
Validation: Matthew Lees, Ryan Smith
Writing – original draft: Matthew Lees
Writing – review & editing: Matthew Lees, Rosemary Knight, Ryan Smith

Prior to the 2000s, subsidence was monitored through leveling surveys, which measured the total subsidence at the surface with limited spatial and temporal resolution, and installation of extensometers, which measured the aquifer system compaction over discrete depth intervals in wells. In the past two decades, the widespread availability of satellite geodetic sensing from Global Positioning Systems (GPS) and interferometric synthetic aperture radar (InSAR) has allowed us to observe the subsidence at an unprecedented level of detail (Chen et al., 2015; Farr & Liu, 2014; Farr et al., 2015). This imaging capacity has led to a large number of studies which have allowed us to make significant improvements in our understanding of the broad-scale features of the subsidence, including its relation to different land uses (Jeanne et al., 2019; Levy et al., 2020), groundwater and surface water flow patterns (Neely et al., 2021), losses in the amount of stored groundwater (Chaussard & Farr, 2019; Faunt et al., 2016; Liu et al., 2019; Ojha et al., 2018, 2019; Smith et al., 2017), the depths at which the compaction originated (Carlson et al., 2020; Vasco et al., 2019) and the origin of groundwater contaminants (Smith et al., 2018). In addition to the geodetic data, these studies have typically utilized complementary Valley-wide data sets along with some local-scale measurements such as hydraulic head. These approaches, enabled by satellite geodetic sensing, have resulted in major advances in our understanding of subsidence.

Using satellite geodetic measurements to understand land subsidence, however, has a few limitations. In particular, the geodetic measurements observe only the total, integrated surface deformation and do not provide any direct information on the depths at which compaction occurs in the subsurface. Several studies have attempted to address this limitation using geophysical inversion methods (Carlson et al., 2020; Vasco et al., 2019) or numerical modeling (Smith et al., 2021). A second limitation is that the geodetic record, and particularly the InSAR record, is still relatively short compared to the time scales over which residual compaction of clays is thought to occur. The earliest literature-reported InSAR measurements of the SJV are from 2002 (Smith & Knight, 2019), and Farr and Liu (2014) suggest that reliable coverage only began in 2006. This limitation might be significant because modeling studies have reported time scales for the residual compaction of clays ranging from 5 to 1,400 years (Helm, 1978; Ireland et al., 1984), which far exceeds the duration of the geodetic record. Finding approaches which enable geodetic measurements to address the depths at which compaction occurs, as well accounting for the long time scales over which residual compaction can continue, is an important issue in advancing subsidence science in the SJV.

Integrating the geodetic measurements with a physical model of subsurface compaction presents a way to understand both the depths at which compaction occurs and the long-associated time scales. Our best conceptual model of subsidence in alluvial aquifer systems such as the SJV is the aquitard-drainage model, which describes how a head fall in the coarser-grained regions of aquifers causes the gradual drainage of water from the clay interbeds within aquifers and the confining layers separating them, resulting in the head drops which cause subsidence (Holzer, 1998; Liu & Helm, 2008). One numerical implementation of this model, which has been successfully applied in the SJV and elsewhere, is referred to as a 1D compaction model (Helm, 1975; Hung et al., 2012). In a 1D compaction model, the evolution of head in the coarser-grained aquifer sediments is assumed to be known, either through direct measurement or by simulation in a groundwater model. The model then solves for the gradual drainage of the clay interbeds and confining layers, and calculates the resulting compaction. Since such a model can be applied to simulate both compaction in multilayered aquifer systems and the residual compaction of clays within the aquifer/s, it has the potential to address both limitations of geodetic data raised in the previous paragraph, and is the approach we take in this paper.

1D compaction models have been applied in the SJV in three main ways. First, in the 1970s, they were used by Helm to simulate compaction over depth intervals monitored by extensometers (Helm, 1975, 1976, 1977, 1978). These models, which took measurements of hydraulic head in coarser-grained regions and compared the simulated compaction to that directly measured by extensometers, were accurate and provided important insights into the nature of subsidence, but can only be applied where there are extensometers. This is a major drawback as the extensometer network in the SJV has largely fallen into disrepair since the 1980s (Swanson, 1998), and the subsiding region has changed such that surviving extensometers are no longer in the areas of greatest concern (Figure 1). Second, 1D compaction models have been used in conjunction with groundwater flow models which simulate the head in the coarser-grained regions. A drawback of this approach is that, since volumes of pumped groundwater in the SJV are rarely measured and not publicly reported, the groundwater flow models have to make various assumptions about the fluxes of water in and out of the aquifer system to estimate hydraulic head. Furthermore, regional-scale models are computationally expensive, often controlled by tens to hundreds of

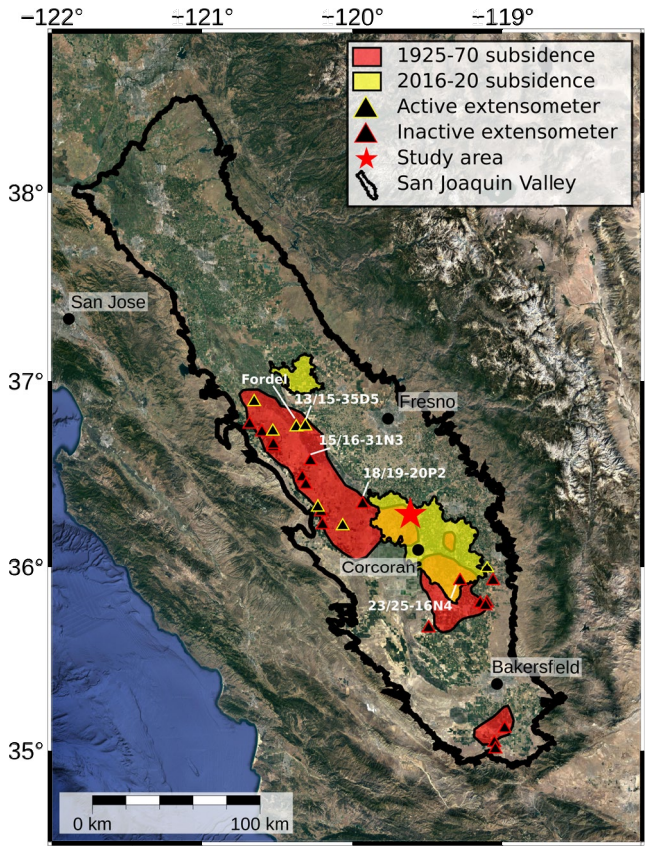

Figure 1. Map showing the relationship between 1925 and 1970 subsidence, 2016–2020 subsidence, and the location of extensometers. There are almost no active extensometers in the regions which subsided between 2016 and 2020, which also contains our study area (shown by the red star). The 1925–1970 subsidence is defined as the region which subsided by 120 cm (4 feet), taken from Ireland et al. (1984), while 2016–2020 subsidence is the region which subsided by 50 cm during the five water years 2016–2020, as measured by the Sentinel InSAR data described in Section 3.3.1. Extensometer locations are gathered from the USGS's California Water Science Center (https://ca.water.usgs.gov/land_subsidence/central-valley_extensometer-data.xlsx), from the data set associated with Faunt (2009) and from Poland et al. (1975). Five important extensometers, which are referred to later, are labeled with their names.

calibration parameters, and simulate multiple complex processes in addition to subsidence. For these reasons, it is challenging to accurately characterize subsidence with them, although they can capture broad-scale subsidence patterns (Corbett et al., 2011; Faunt, 2009; Williamson et al., 1989).

The third way 1D compaction models have been used, which is the focus of this paper, is to use measurements of hydraulic head and compare simulation results with *integrated* measurements of subsidence, such as those made by InSAR. These models have the advantage of not relying on auxiliary modeling assumptions to obtain head inputs, and can be applied wherever satellite geodetic and head data are available, without being tied to locations with extensometers. To date, we are aware of only one published study applying such a model in the SJV (Smith & Knight, 2019). This study demonstrated the viability of the method and was able to make important predictions about how future head changes would influence subsidence. However, their study did not simulate subsidence prior to 1990 or make a distinction between compaction occurring in the upper aquifer, lower aquifer, and Corcoran Clay, largely due to difficulty in obtaining the high-quality head inputs necessary to do so. If such inputs could be obtained, these models would be able to provide even more valuable insights into the nature of subsidence.

Our objective in this study is to develop a model, similar to that of Smith and Knight (2019), but one which covered a longer time span and was able to distinguish between compaction in the three major hydrostratigraphic layers. In particular, we wanted to see whether such a model would reproduce the long time scales for residual compaction of clays obtained by historic modeling studies (10s–100s of years). The potential long time scales provided the incentive to model over a longer time span since they suggest that residual compaction of clays initiated in the 1920s could still be occurring today. Another specific goal was to constrain the amount of compaction in each of the upper aquifer, lower aquifer, and Corcoran Clay in a location without extensometers, as we lack direct observational data on this in the currently subsiding regions (Figure 1). Implementing a 1D compaction model in the Valley over a long time scale and separately treating the three aquifer system layers represents a significant advance over previous work; the reason this has not been attempted before is largely due to the difficulties in obtaining a long record of head in the coarser-grained sediments in both the lower and upper aquifers.

We focused on the Tulare Lake and Kaweah groundwater subbasins, where we had existing relationships with local partners which provided access to very long head records and the auxiliary information required to assign the head records to the aquifer-of-origin. We identified a small study area within those subbasins in which to target our modeling. Although we worked at a single study area, the approach we have developed is readily applicable for studies in other regions of the SJV, and even alluvial aquifer systems worldwide. Additionally, we expect many of our conclusions on the nature of compaction at our study area to be transferrable throughout the SJV due to a shared hydrostratigraphy and head history, and can therefore provide an important part of the scientific endeavor to provide better information on Valley-wide subsidence.

2. Background: Governing Equations

The standard numerical implementation of the aquitard-drainage model was first set out in Helm (1975). Here, we summarize the key parts of the theory in order to highlight the governing equations which we used in our model and the key dynamics which they capture.

Helm (1974) derived the governing equation for the draining of clay layers in terms of effective stress, σ', which is related to head h by $\sigma' = \sigma - \rho g h$, where σ is the overburden stress, ρ is the density of water, and g is the gravitational acceleration. When cast in terms of effective stress, the governing equation takes a form well known in mathematics: the diffusion equation. This represents how effective stress changes diffuse into the clay layers. The equation is produced below:

$$\frac{K_v}{S_s}\frac{\partial^2 \sigma'}{\partial z^2} = \frac{\partial \sigma'}{\partial t} \tag{1}$$

In Equation 1, K_v is the vertical hydraulic conductivity and S_s is the specific storage, which itself can be written as the sum of the skeletal specific storage S_{sk} and the specific storage due to the compressibility of water S_{sw} ($S_s = S_{sk} + S_{sw}$). Working in effective stress requires knowledge of the overburden stress. In certain special cases, it may be possible to assume that overburden stress is constant with time, but this is not the case in the multilayered aquifer system of the SJV, where it varies in all three aquifer system layers (two aquifers and the confining layer) based on the upper aquifer head. We calculated this variation using the relation $d\sigma = \rho g d h_{upper} S_y$ where S_y is the specific yield, which is explained in Poland et al. (1975).

The effective stresses of the two aquifers are time-varying and act as boundary conditions for Equation 1. These boundary conditions drive the system's dynamics. The terminology "interbed" is used to describe a clay layer embedded within an aquifer, whereas "confining layer" describes a clay layer which separates two aquifers. For interbeds, the boundary conditions are the same on the upper and lower boundaries. For confining layers, the upper and lower boundary conditions are different, and are the effective stress in the overlying and underlying aquifers, respectively. Equation 1 can be solved by standard methods for solving partial differential equations; in this study, we used a finite-difference method.

An important part of the solution of Equation 1 is the hysteretic behavior of S_{sk}. As proposed by Helm (1975), this can be approximated by two values, depending on the effective stress: a so-called elastic value (S_{ske}), which is relatively small and applies when effective stress is below its historic maximum; and a so-called inelastic value (S_{skv}), which is far larger and applies when effective stress is at its historic maximum. Mathematically, we followed Helm in applying this in our model as follows:

$$S_{sk} = \begin{cases} S_{ske} \text{ if } \sigma' < max\,(\sigma') \\ S_{skv} \text{ if } \sigma' \geq max\,(\sigma') \end{cases} \tag{2}$$

Calculation of compaction for each clay layer was computed according to Equation 8 in Helm (1975). We reproduce that equation here, modified slightly to match our notation:

$$b\,(t_i) = \frac{\Delta z}{\rho g}\left[S_{\mathrm{skv}} \sum_{j=1}^{j-1}\left(\max_{n \leq i}\left(\sigma_j'^{n}\right) - \sigma_j'^{0}\right) - S_{\mathrm{ske}}\left(\max_{n \leq i}\left(\sigma_j'^{n}\right) - \sigma_j'^{i}\right)\right] \tag{3}$$

where $b\,(t_i)$ refers to the total compaction of a clay interbed or confining layer at timestep i, Δz is the mesh spacing, and there are J nodes. Superscripts on effective stress refer to the value at a given timestep. The nodes used were the midpoints of the nodes used to solve Equation 1; values of effective stress at the midpoints were obtained through linear interpolation. Note that, in the condition that effective stress at the current timestep is equal to its maximum, the S_{ske} term equates to zero and compaction is calculated purely as the inelastic sum.

An important aspect of Equation 1 is the existence of a time constant which represents the characteristic time over which diffusion of effective stress occurs. (See Hoffman et al. (2003) for a derivation.) This time constant represents the time taken for the effective stress within a clay, with constant initial stress, to achieve 93% equilibration to a step-change in the boundary condition and is written as:

$$\tau = \frac{b_0^2 S_{sk}}{4K_v} \tag{4}$$

where b_0 is the initial thickness of the clay layer. This time constant provides a useful guide to understanding the time scales over which compaction occurs. In the case of a clay layer experiencing the historic maximum of

effective stress, $S_{sk} = S_{skv}$ and the time constant is long, which we refer to as the inelastic time constant ($\tau_{inelastic}$). This represents the residual compaction of clays. If the clay layer is not at its historic maximum effective stress, $S_{sk} = S_{ske}$ and the time constant, which we now call the elastic time constant ($\tau_{elastic}$), is shorter. In reality, clay layers seldom satisfy the conditions required for Equation 4 to represent the time to reach 93% equilibration. In particular, clay layers almost never have a constant initial head and boundary conditions do not have step changes. Additionally, there are typically parts of a clay layer experiencing their historic maximum of effective stress and other parts which are not. Even in these scenarios, τ remains a meaningful time constant, since a simple scaling analysis of the diffusion equation (shown in Appendix A) shows that the governing time scale is proportional to τ, provided b_0 is now thought of as the thickness of the clay experiencing a given S_{sk} value and not the entire clay layer. The time constant τ therefore provides a useful rule of thumb for understanding the time scales of expansion/compaction.

Equation 4 applies to an individual clay layer, but it is also useful to also have a time scale which is representative of the entire aquifer system. For this purpose, Helm (1978) suggested a gross time constant, which we will denote $\overline{\tau}$, as defined in Equation 5. The gross time constant for an aquifer system can be thought of as the aggregate time over which residual compaction of clays occurs. Since the aquifer system contains many interbeds of different thicknesses, it is important to note that significant compaction can still occur beyond the gross time constant. In this study, we used the gross time constant to characterize the compaction time scale for our simulations

$$\overline{\tau} = \frac{b_{eq}^2 S_{skv}}{4K_v}$$
$$b_{eq} = \sqrt{\frac{1}{\sum_i n_i} \sum_i n_i t_i^2} \tag{5}$$

Equation 5 applies to an aquifer system containing i unique interbed thicknesses t_i, with n_i interbeds of each thickness. To be consistent with the results of Helm (1978), we did not include confining layers (i.e., the Corcoran Clay) when computing the gross time constant.

3. Methods

The defined objective of our modeling was to assess the depths and time scales over which compaction occurs. We included three steps in our methodology to answer these questions, which are described in Sections 3.1–3.3:

3.1. Selection of a Study Area

We required a study area where we had access to a long head record in both the upper and lower aquifers, ideally stretching back to the onset of subsidence. It quickly became apparent that nowhere in the SJV does a single well or well cluster contain such information, and that we would have to stitch together the records from multiple wells. We selected a study area based on a group of eight wells just south of the town of Hanford, which, when taken together, allowed us to reconstruct head records in both aquifers from 1952 to 2017. The location of our study area within the SJV is shown in panel a of Figure 2. Literature records showed major subsidence began in this area in around 1953 (Poland et al., 1975), so we could satisfy our requirement for a long temporal record. To define the exact study area, we applied a 1 km buffer around the eight wells (see panel b of Figure 2 for the study area shape).

In addition to the availability of long-term groundwater-level measurements, our highest priority, there were several other advantages of this study area. Specifically, a continuously monitored, multiscreened well-known as Well H with 4-hourly measurements from 2015 to 2020 lies just outside of our study area and provides important contextual information about head levels. In addition, there are nearby historical subsidence measurements obtained in the 50s, 60s, and early 70s (Poland et al., 1975) as well as a leveling survey location along Highway 198 within a few kilometers of the study area (Sneed et al., 2018). A final benefit of the selected study area was that it contained a borehole, drilled by Kaweah Delta Water Conservation District, with a driller's and resistivity log, which we could use to identify the coarser-grained layers and clays in the subsurface. These measurements, and how we incorporated them into our model, are discussed in detail in Section 3.2. The locations of these other data sets with relation to our study area can be seen in panel b of Figure 2.

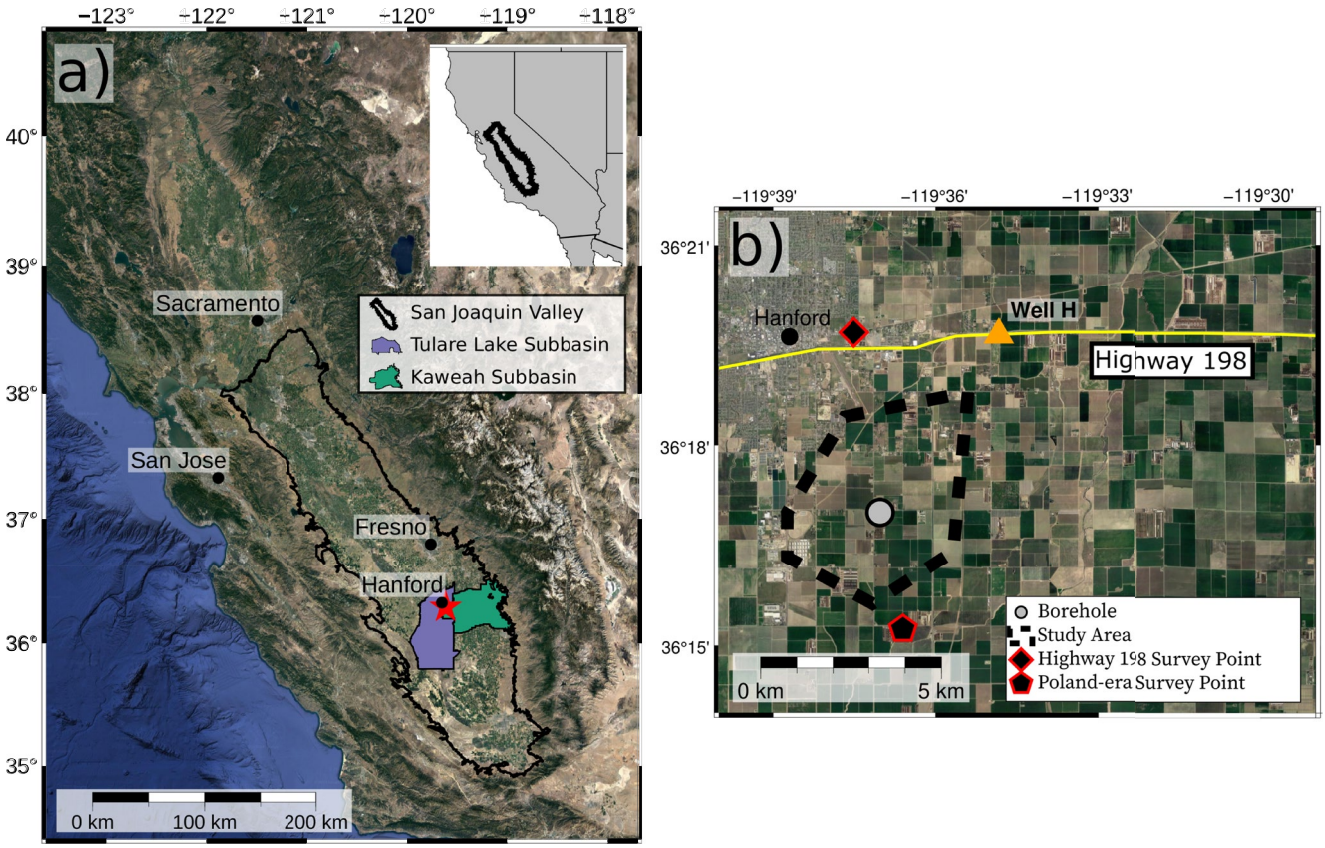

Figure 2. (a) The study area location, shown by the red star, within the San Joaquin Valley (SJV; main); and the SJV within California (inset). The Tulare Lake and Kaweah subbasins are also shown. (b) The study area, shown in detail, and the locations of the borehole, leveling surveys and Well H. The locations of the eight wells which defined the study area are not shown, as some of the well data are private.

3.2. Preparation of Model Input Data

There were five model inputs to prepare. These were:

1. Head time series in the upper and lower aquifers
2. Information on the thickness of clay interbeds and confining layers
3. Defining the top and bottom of the compacting domain
4. The initial effective stress condition in the clay interbeds and confining layers
5. Data on appropriate physical parameters

We describe how we estimated each input in Sections 3.2.1–3.2.5.

3.2.1. Preparing Head Time Series in the Upper and Lower Aquifers

The lack of a head time series, of sufficiently high accuracy with a sufficiently long time-record, is a major impediment to running 1D compaction models and simulating subsidence in the Valley. The creation of the input head time series was what allowed us to develop a model spanning 65 years and simulating compaction in three model layers. It is generally difficult to construct long-term head time series corresponding to the upper and lower aquifers in the SJV. Although Smith and Knight (2019) presumed the same head in the two aquifers, the data from Well H, which were not available to Smith and Knight, reveal significantly different trends and seasonal oscillations in head between the two aquifers (Figure 3). In particular, the seasonal head variations in the lower aquifer are much larger than in the upper aquifer. This is an expected characteristic for a confined aquifer, and we used it to help identify whether other head measurements were from the upper or lower aquifers.

The data from Well H provide an exceptionally high-quality record of head. There are many other wells in the SJV in which hydraulic head is measured, but for the vast majority of these the data are of lower quality and

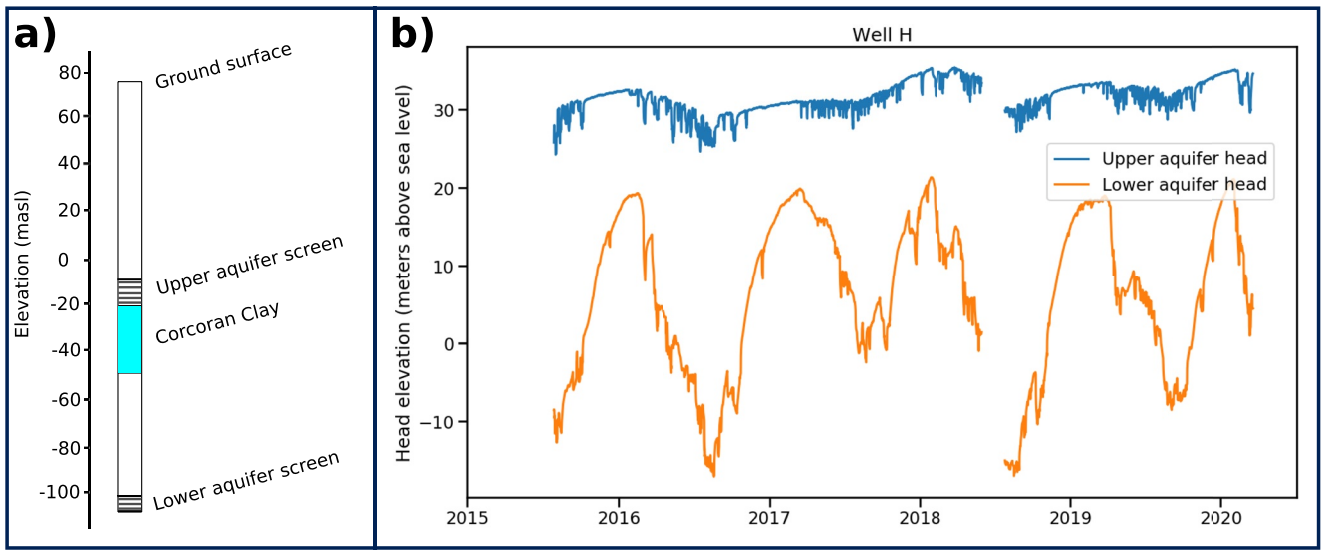

Figure 3. (a) The relationship between the Corcoran Clay and the screened intervals in Well H and (b) the continuously monitored head records from Well H. These two head time series show clear and distinct head values and trends between the two aquifers. The data from Well H were provided by Kings County Water District, who installed and operate the well.

there are numerous challenges in making these data usable. The primary challenges are that well completion reports are seldom available, making it difficult to determine the aquifer that is being sampled; wells are often screened across both aquifers; and measurements are often either privately owned or contain unmarked errors (Brewster et al., 2015). Additionally, the standard measurement frequency is twice per year, with many wells not even achieving that. In our study area, we had access to a large number of head measurements from several sources. The available data sets were: statewide well data from the California Statewide Groundwater Elevation Monitoring (CASGEM) database (California Department of Water Resources, 2021); a complementary local database of water-level measurements in the Kaweah groundwater subbasin, compiled by GSI Water Solutions and provided with the permission of the local groundwater agencies; water-level measurements reported in Poland et al. (1975); and water-level data from Well H (provided by Kings County Water District). Without all of these data sets, it would not have been possible to reconstruct the head in both aquifers over a multidecadal period. In the SJV, we expect that the modeling approach that we used, with multiple aquifer layers, could only be done where there are local partners willing to provide available head data.

To leverage the various sources of head data, we categorized wells in our study area into four classes: gold standard upper aquifer wells, gold standard lower aquifer wells, supplementary upper aquifer wells, and supplementary lower aquifer wells. Gold standard wells were those for which we had very high confidence of which aquifer the head measurements represented. To that end, gold standard upper aquifer wells were defined as those with available well completion information, well depth shallower than the Corcoran Clay, and seasonal amplitude variations similar to those in the upper aquifer at Well H. Gold standard lower aquifer wells were those with well completion information available, perforated intervals exclusively below the Corcoran Clay, and seasonal amplitude variations similar to those in the lower aquifer at Well H. Corcoran Clay depths were determined from the borehole data as described in Section 3.2.2. The two gold standard upper aquifer and two gold standard lower aquifer wells which we identified in our study area are highlighted in Table 1. Unfortunately, using only these four wells would have left a head time series with gaps in the upper aquifer between 1978 and 2010 and gaps in the lower aquifer between 1981 and 2006. We identified supplementary wells to fill these gaps.

Supplementary wells were additional wells which did not have completion information available but satisfied other criteria to give us confidence of the aquifer which they were recording. Supplementary wells were defined as those with head measurements which showed overlap with those from gold standard wells, and which showed seasonal amplitude variations similar to the corresponding aquifer at Well H. We identified two supplementary wells in each aquifer which, when combined with the gold standard wells, gave a continuous record of measurements from 1952 to 2017, shown in Figure 4. The precise locations of the wells used are not shown, since some of

Table 1
Information on the Wells Used to Create Input Head Time Series

Well name(s)	Data source(s)	Well depth (m) [elevation of well base]	Screened interval depth [elevation]	Period of coverage	Classification
Upper aquifer wells					
UA1/19S22E19A002M	CASGEM, Poland et al. (1975)	34 [32 masl]	NA	1951–1978	Gold standard upper aquifer well
UA2	*Local head data set*	*108 [−39 masl]*	*96–108 [−27 to −39 masl]*	*2010–2017*	*Gold standard upper aquifer well*
UA3/19S22E04M001M	CASGEM, local head data set	N/A	N/A	1971–2017	Supplementary upper aquifer well
UA4	Local head data set	N/A	N/A	1987–2017	Supplementary upper aquifer well
Lower aquifer wells					
LA1/19S22E08D002M	Local head data set and CASGEM	149 [−80 masl]	136–149 [−67 to −80 masl]	2006–2019	Gold standard lower aquifer well
LA2/19S22E19A001M	Poland et al. (1975) and CASGEM	N/A	170 [−104 masl]	1952–1981	Gold standard lower aquifer well
LA3	Local head data set	N/A	N/A	1987–2017	Supplementary lower aquifer well
LA4	Local head data set	N/A	N/A	1970–2013	Supplementary lower aquifer well

Note. Well name refers to the encoded name used for the purposes of this paper (UA1-4 and LA1-4; UA stands for upper Aquifer and LA for Lower Aquifer). Where the well data are publicly available, the California State well number is also given under well name, but for certain wells from the local head data set, the head measurements are not publicly available so we have only provided the encoded name. Gold standard wells have gold shading. The italics for Well UA2 indicates that this well was eventually excluded due to anomalous measurements. Well depths and screened intervals are given both as depths and elevations.

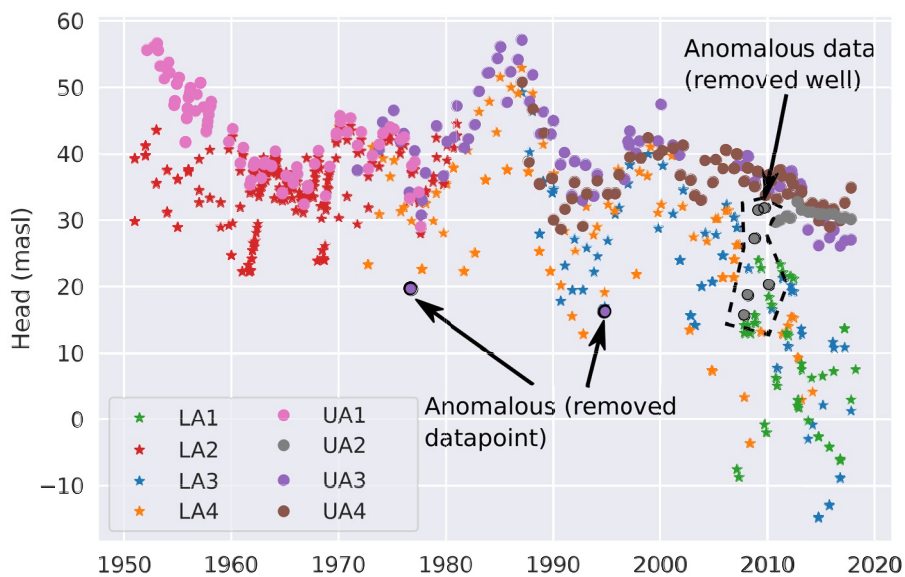

Figure 4. All well data from the gold standard and supplementary wells, giving continuous coverage in both aquifers from 1952 to 2017. Well names are given as encoded names (UA1, UA2, etc.) as described in the caption for Table 1. The anomalously low measurements that were removed are circled in thick black and are labeled, as are the anomalous measurements which led to the removal of Well UA2. For discussion of the anomalous data, see the main text.

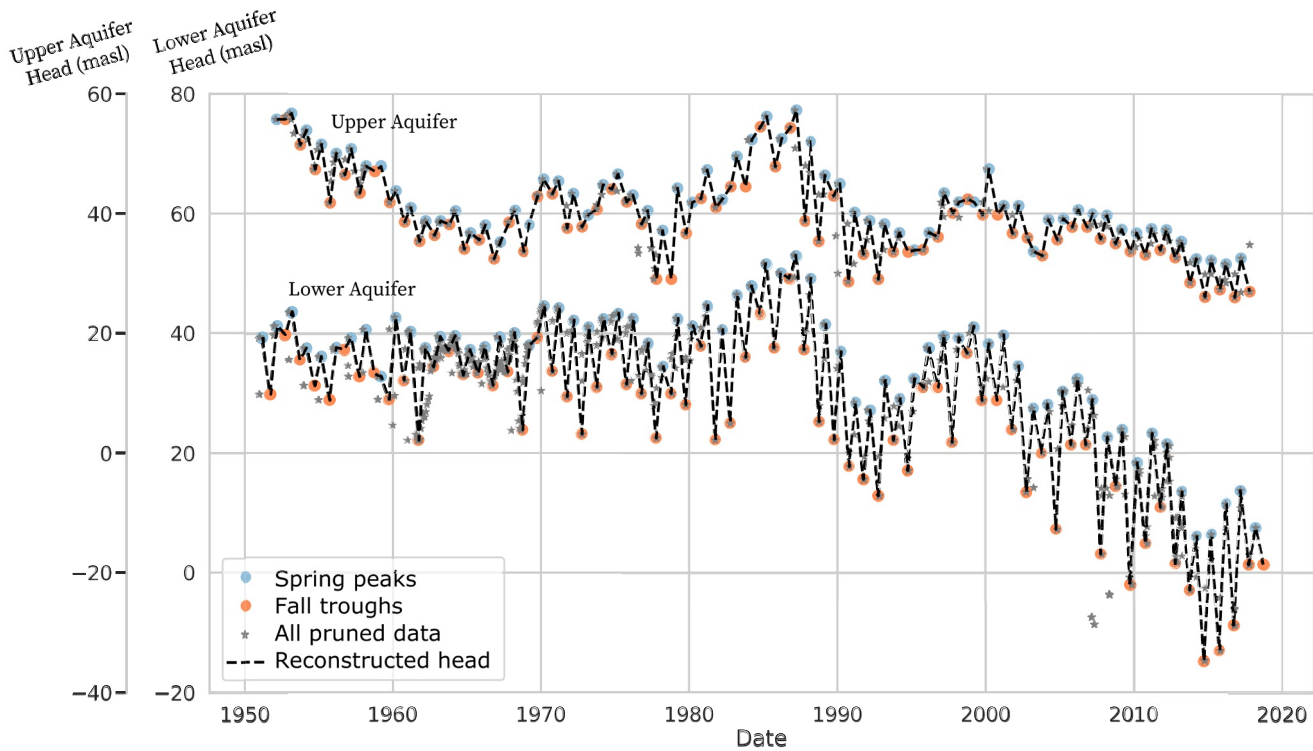

Figure 5. The interpolated head data used as model input, plotted on top of the Spring peaks, Fall troughs, and raw data used to construct the input.

the measurements from the local head data set are not publicly available. However, all wells are within the study area shown in panel b of Figure 2; the study area was defined by a 1 km buffer around these wells.

To convert the well head measurements into model input for each aquifer, we took several additional steps. First, we dealt with some anomalies in the well data. Well UA2 had a number of anomalously low head measurements in 2007–2010 which we could not readily explain; we therefore acted conservatively and removed this entire well. Additionally, we removed two measurements taken in 1995 and 1976 from UA3 which were also anomalously low, but since these were only two measurements across a 45-year record, we did not exclude the entire well (Figure 4). Next, using the remaining head measurements, we extracted a Fall minimum and Spring maximum for each year, then linearly interpolated between those measurements to create continuous time series. For each year, we defined the Fall minimum as the minimum datapoint between the months of August and November (inclusive), and we defined the Spring maximum as the maximum datapoint between the months of January and May (inclusive); in the extremely rare case that no data were available within Spring or Fall, we used the measurement from the previous year (for instance, upper aquifer Fall 1977 and Fall 1976 are identical for this reason). The final, resulting time series used as model input are presented in Figure 5.

3.2.2. Preparing Information on the Thickness of Clay Interbeds and the Corcoran Clay

To identify the thickness of clay interbeds and the top and bottom of the Corcoran Clay we used the driller's and resistivity logs made in the borehole in our study area, provided to us by Kaweah Delta Water Conservation District. The borehole was 210-m deep and both logs spanned its entire depth. The driller's log contained generalized lithologic descriptions of the subsurface at 5-foot intervals but did not describe individual clay interbeds. The resistivity log was a 16-inch normal log.

We interpreted the resistivity log by presuming that clays are the least resistive layers and applying resistivity cutoffs. These resistivity cutoffs were values below which we assumed the sediments to be clay. To choose appropriate cutoff values, we applied trial cutoffs and compared the result with the identification of the Corcoran Clay and thicker clay interbeds from the driller's log. We determined that the smallest and largest cutoffs which gave good agreement were 30.5 and 38.5 Ω m, respectively, this is shown in panels a and b of Figure 6. There was no variation in the depths to the top or bottom of the Corcoran Clay across this range, which we therefore took

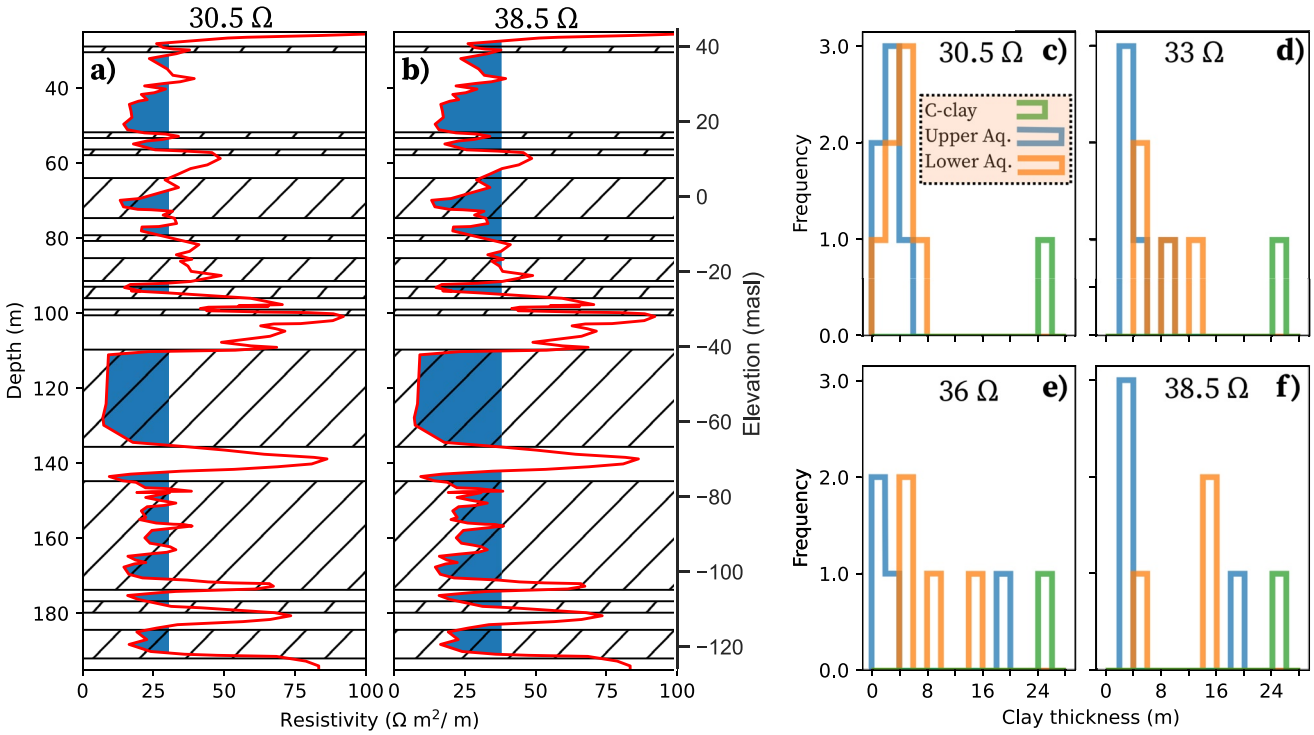

Figure 6. (a and b). Two plots showing the resistivity log (red curve), the clay layers deduced from the driller's log (hatched shading), and the clays identified when applying resistivity thresholds of 30.5 and 38.5 Ω ms, respectively. The region to the left of the threshold is shaded in blue. The Corcoran Clay is between 108 and 135 m depth (−40 and −67 masl). (c–f) The four versions of the clay distributions which were obtained from applying the four different cutoffs.

as 108 and 135 m, respectively. However, there was variation in the number and thickness of clay interbeds in each aquifer. In order to represent this variation, we additionally considered two intermediate cutoffs of 33 and 36 Ω m. The four resulting distributions showing the thickness of the clay interbeds and the Corcoran Clay are shown in panels c–f of Figure 6.

One complication encountered in the modeling was that the lower aquifer often extended below the base of the borehole (see Section 3.2.3 for discussion of the base of the lower aquifer). When faced with this situation, on the basis that there is no evidence for a change in depositional environment below the log, we scaled the number of clays from within the log to correspond to the lower aquifer thickness. For example, the log covered a 50-m thick region of the lower aquifer; in a simulation with a lower aquifer thickness of 100 m, we doubled the number of clay interbeds identified in the log.

3.2.3. Defining the Top and Bottom of the Compacting Domain

When simulating compaction over an interval and comparing with measured extensometer data, it is trivial to define the compacting domain since it is simply the depth interval covered by the extensometer. However, when comparing with deformation measured at the ground surface (so integrated over all compacting depth intervals), as in this study, it is necessary to define the domain over which compaction is occurring.

First, we needed to define the top of the compacting zone. The aquitard-drainage model does not currently account for the situation where material becomes unsaturated. We therefore elected to define the top of the compacting zone as the top of the permanently saturated region which is at a depth of 41 m, i.e., the depth of the upper aquifer head in 2017. The water table declined by about 25 m between 1952 and 2017 so it is possible that there was some contribution to compaction from this drained region of the aquifer but extensometer data indicate that shallow compaction contributes only a small portion of the total subsidence (Ireland et al., 1984). We therefore considered it reasonable to omit this region from the model.

Next, we needed to define the base of the compacting zone, which occurs in the lower aquifer. We defined the compacting zone in the lower aquifer as the region over which significant head changes occur in the

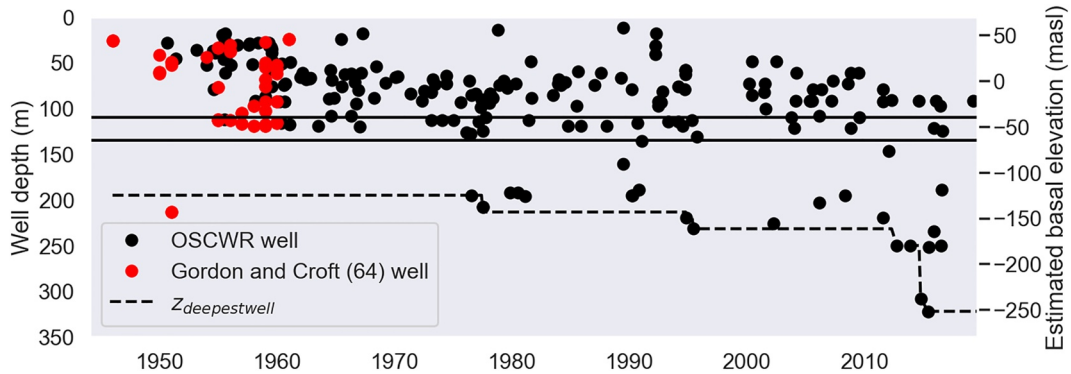

Figure 7. Well completion records showing the drilling of new wells from 1952 to 2017 in our study area. The data were obtained from the OSWCR database and from Gordon and Croft (1964). The two solid horizontal lines show the top and bottom of the Corcoran Clay at the borehole location. The dashed line is the time-varying trace of the depth to the deepest well. The elevation of the well's base (basal elevation) is shown on the right *y*-axis and was estimated by assuming an elevation of the land surface of 70 m. Note that, prior to 1969, it was not mandatory for completion reports of new wells to be submitted. The deep well reported in the Gordon and Croft (1964) data from 1952 was the well we used to observe head measurements; we believe this was not a pumping well and have therefore excluded it from our deepest well trace.

coarser-grained sediments. Smith and Knight (2019) used a similar definition, and assumed the base of compacting material aligned with a low-resistivity unit, assumed to be a thick clay, imaged with airborne electromagnetics. They solved for a cutoff term defining the exact location of this boundary, which they varied until simulated subsidence agreed with observational data. We took a slightly different approach, as we did not have access to resistivity data deeper than the borehole in our study area. Instead, we based our approach on data providing the depths of drilled wells from the California Department of Water Resources' Online System for Well Completion Reports (OSWCR). Since mandatory well reporting was only introduced in 1969, we additionally digitized data from Gordon and Croft (1964) to reveal the depths of drilled wells pre-1969.

The OSWCR data allowed us to identify the deepest drilled well in our study area. We expected head changes in the coarser-grained sediments to propagate for some depth below this, depending on the hydraulic conductivity of the lower aquifer and the time scale being considered. From resistivity logs, an impermeable layer called the San Joaquin Formation has been identified in our study area at about 800 m below the surface (approximately −730 masl) which we considered to be the maximum possible depth to which head changes could propagate. This layer is shown, e.g., in Figure 14b in the Mid Kings River GSP (El Rico Groundwater Sustainability Agency et al., 2020). However, to accurately determine the propagation of head changes in the region between the base of wells and the San Joaquin Formation would require a detailed hydrogeologic model in a region for which we had neither head measurements for validation nor well data to describe the subsurface structure. Instead, we made the simple approximation that head changes in the lower aquifer propagated for some depth-of-influence d_i below the deepest pumping well. Since we could not reliably know d_i, we allowed a range of values from 50 to 200 m. The base of the lower aquifer (z_{base}) in our model was therefore defined as $z_{base} = z_{deepestwell} + d_i$, where $z_{deepestwell}$ is the depth to the base of the deepest drilled well. Unlike in the previous hydromechanical modeling studies of Helm (1975) and Smith and Knight (2019), this approach gave us a temporally varying base of the lower aquifer, since $z_{deepestwell}$ has increased as more wells were drilled over time, as shown in Figure 7. We read values for $z_{deepestwell}(t)$ from Figure 7 as follows: $z_{\text{deepestwell}}$ = [1952–1977: 195 m, 1977–1995: 208 m, 1995–2011: 233 m, 2011–2014: 250 m, 2014–2017: 323 m]. We therefore had the base of the lower aquifer ranging between depths of 245 and 523 m (elevations of approximately −175 to −425 masl), which is similar to the depth range of 220–450 m found by Smith and Knight (2019).

As well as the above description, a diagram illustrating the model hydrostratigraphy, including the base of the lower aquifer, is shown in Figure S1 in Supporting Information S1.

3.2.4. The Initial Effective Stress Condition in the Clay Interbeds and Confining Layer

Given the long reported time constants for the residual compaction of clays, we expected the initial effective stress condition inside the clay interbeds and confining layers to be an important input variable. Although the

Table 2
The Values of Physical Parameters Used in Our Simulations

Nonvarying parameters		
Parameter name	Value used in model	Source
S_{sw}	1.5×10^{-6} m^{-1}	Smith et al. (2017)
ρ	1,000 kg m^{-3}	N/A
g	9.81 m s^{-2}	N/A
S_{ske}^{cl}	1.35×10^{-5} m^{-1}	Faunt (2009)
S_{ske}^{co}	4.8×10^{-6} m^{-1}	Faunt (2009)
S_y	0.2	Faunt (2009)
Varying parameters		
Parameter name	Literature range and source(s)	Upper and lower bounds
K_v	1.1×10^{-6} to 1.4×10^{-2} m day^{-1} from Faunt (2009) and Smith and Knight (2019)	2.5×10^{-7} and 3.00×10^{-6} m day^{-1}
S_{skv}	4.6×10^{-4} to 2.9×10^{-3} m^{-1} from Faunt (2009) and Smith and Knight (2019)	6×10^{-4} and 3.0×10^{-3} m^{-1}

initial hydraulic head condition within clays interbeds and aquitards cannot be measured, Helm (1975) suggested that it can be estimated based on the prior history of head in the aquifers. We chose to use the aquifer head history to bound the initial condition, rather than make a single estimate. We assumed that the initial head profile in the clay interbeds were constant within each aquifer, and we denote the initial head in clay interbeds in the upper aquifer as h_0^{upper} and in the lower aquifer as h_0^{lower}. We bounded these by considering what was known about head levels pre-1952.

In the upper aquifer, we identified CASGEM well with state well number 19S22E06N001M within the study area which contained head data from 1925 to 1963. This well showed head approximately constant at a value of 68 masl from 1925 to 1948. From 1948, it dropped steadily to its 1952 value (55 masl). We therefore bounded h_0^{upper} between 55 and 68 masl.

In the lower aquifer, we were unable to identify any wells providing head data prior to 1952. Instead, we used the literature to obtain information, albeit limited, about lower aquifer head levels. In a map representing the location of artesian wells in 1905, Mendenhall et al. (1916) included our study area within the artesian zone. This gives us reason to believe that lower aquifer head in our study area was at least the level of the land surface, or 71 masl, in 1905. By 1925, Harding (1927) reported that artesian wells in the Valley had stopped flowing apart from in very wet winters, which suggests head was at or below 71 masl by that point. We do not, however, have any constraint on the deep aquifer head between 1925 and 1952. We therefore bounded h_0^{lower} as being between the 1952 level (39 masl) and the land surface (71 masl).

Within the Corcoran Clay confining layer, we defined a linear initial head profile with the initial head on the upper edge of the Corcoran Clay set equal to h_0^{upper} and on the lower edge set equal to h_0^{lower}. This is the expected head profile within a confining layer in equilibrium with the surrounding aquifers.

3.2.5. Preparing Values for the Physical Parameters

In the model equations described in Equations 1–3, there are seven hydrologic parameters: vertical hydraulic conductivity of clays K_v, elastic skeletal specific storage of clays and of coarser-grained sediments (denoted here as S_{ske}^{cl} and S_{ske}^{co}, respectively), inelastic skeletal specific storage of clays S_{skv}, the specific storage due to the compressibility of water S_{sw}, the density of water ρ and the acceleration due to gravity g. Additionally, an eighth parameter (specific yield S_y) is needed to calculate overburden stress. Three of these parameters (S_{sw}, ρ, and g) are well-known physical constants, while specific yield has a relatively tightly constrained value in the SJV (Faunt, 2009). Additionally, since $S_{ske}^{cl} \ll S_{skv}$ and $S_{ske}^{co} \ll S_{skv}$, we did not expect S_{ske}^{cl} or S_{ske}^{co} to have significant influence on our simulated subsidence, and we therefore did not consider a range of values for these parameters. The values used for these six, nonvarying parameters are given in the top part of Table 2.

The remaining two variables (K_v and S_{skv}) were important to our simulations. Since a range of values for these parameters can be found in the literature, we defined the upper and lower bounds for each of these variables. When defining the bounds for S_{skv}, we only considered values from previous models, as opposed to values from laboratory experiments, as it is known that the values are not comparable at these two scales (Sneed, 2001). The literature ranges and the values used in our simulations are given in the bottom part of Table 2.

3.3. Model Calibration

Many of our model inputs had some uncertainty, or were only defined within upper and lower bounds. Our approach was to perform a grid search, running the model for all possible combinations of input parameters, and then calibrating the resulting simulations with the available observational data of subsidence. We wanted to calibrate our simulations against as many independent data sets as possible. Although there were no extensometers in or near our study area, we had four calibration data sets available to us. These are described below, as well as our approach to defining the acceptance criteria.

3.3.1. 2015–2017 InSAR Data

The 2015–2017 InSAR data were acquired with the European Space Agency Sentinel satellite and processed by TRE Altamira under contract with the California Department of Water Resources (DWR) and are available at https://data.cnra.ca.gov/dataset/tre-altamira-insar-subsidence. The data provided measurements of vertical displacement every 6–12 days, starting in February 2015 and continuing until the end of our study period, at the pixel locations seen in Figures 8a and 8b. TRE Altamira obtained vertical displacement by combining information from line-of-sight measurements taken in both ascending and descending orbital directions (TRE ALTAMIRA Inc., 2020). Since our model input head was based on a Fall minimum and a Spring maximum for each year (i.e., temporal resolution of 6 months), we degraded the temporal resolution of the calibration data from 6 to 12 days to annual by using October-to-October values, and used the subsidence between those dates in our calibration. We calibrated our simulated subsidence over two water years: Water Year 2016 and Water Year 2017. Based on previous work, we knew that these years show quite different subsidence rates, so calibrating to both was important to ensure the robustness of our model (Murray & Lohman, 2018). The acceptance criteria for these 2 years were:

Water Year 2016: Simulated annual subsidence between 20 and 34 cm, which was the range of measured subsidence at the pixels in our study area (Figure 8a).

Water Year 2017: Simulated annual subsidence between 9 and 15 cm, which was the range of measured subsidence at the pixels in our study area (Figure 8b).

Note that the estimated accuracy of the 2015–2017 InSAR measurements, obtained through validation against independent cGNSS stations, is 18 mm with 95% confidence (Towill Inc., 2021), which is substantially smaller than the spatial variation in our study area in either 2016 or 2017. The 2015–2017 subsidence time series are shown in Figure S2 in Supporting Information S1, with the 1 October–1 October subsidence used in the calibration annotated.

3.3.2. 2007–2010 InSAR Data

The 2007–2010 InSAR data were the ALOS data described in Smith and Knight (2019). Although the raw ALOS data contained 15 measurements from between 1 June 2007 and 2 July 2010, we elected to use the mean rate of subsidence over that period for our calibration because this long-term estimate of subsidence gave a more reliable estimate of the actual subsidence than the individual measurements, which likely contain some noise. The acceptance criterion between these dates was a mean subsidence rate between 7.0 and 16 cm/yr, which was the range of measured subsidence in our study area. (This range is shown visually in Figure 8c.) Smith and Knight (2019) estimated the error on these InSAR measurements to be 1 cm, which is substantially smaller than the spatial variation in our study area.

In producing this data set, LOS deformation was converted to vertical by dividing the LOS deformation by the cosine of the incidence angle. In doing so, it was assumed that all deformation observed in the LOS was vertical. This assumption was also made by Smith and Knight (2019) on the basis that there is no significant horizontal motion due to tectonic activity (Smith et al., 2017). This assumption could introduce some uncertainty if there

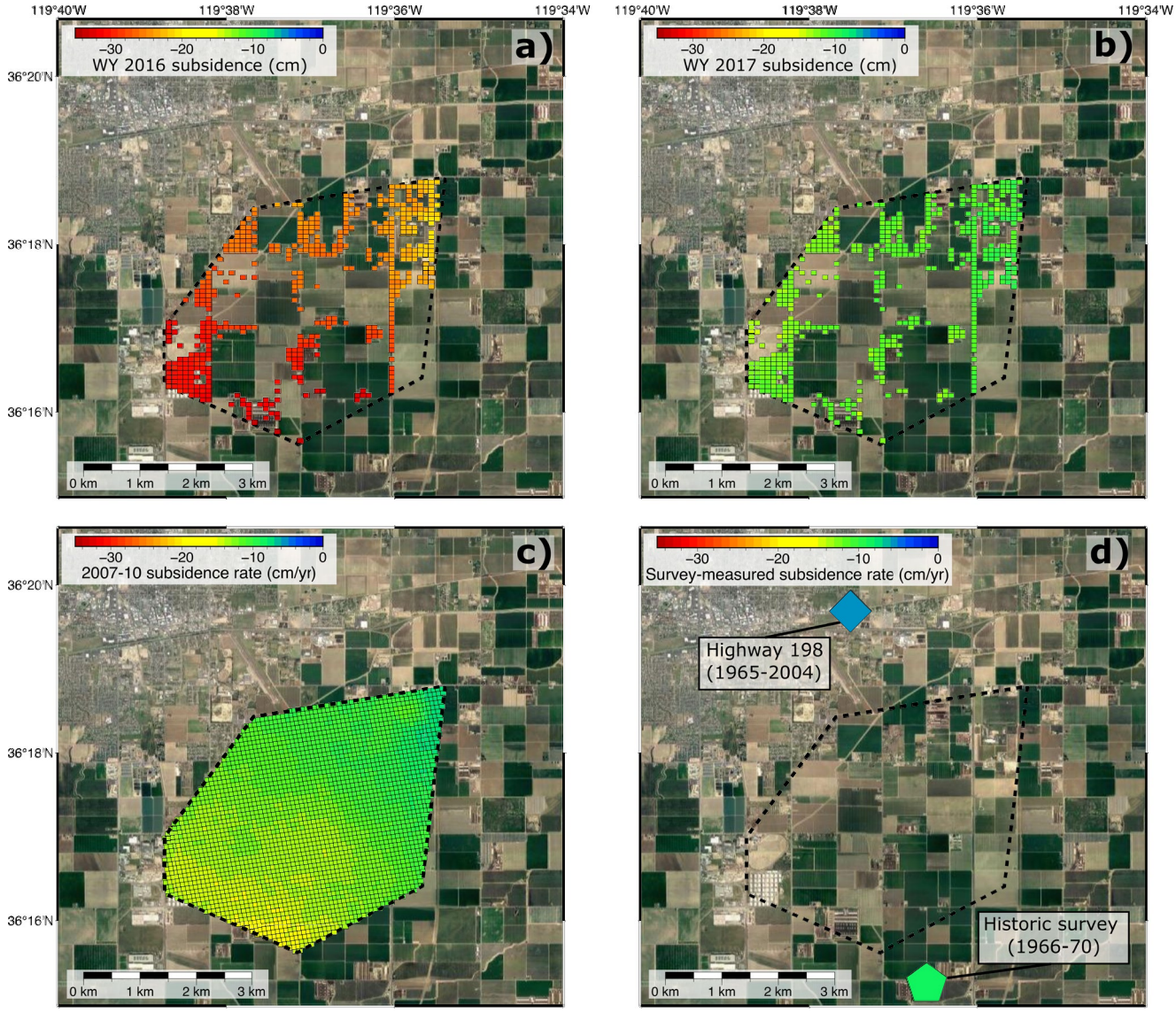

Figure 8. (a). The Water Year 2016 subsidence observed in our study area; (b) the Water Year 2017 subsidence observed in our study area; (c) the 2007–2010 subsidence rates observed in our study area; (d) the subsidence rates observed outside our study area at the Highway 198 and historic survey points. In all panels, the study area is shown as the black dashed outline, and InSAR pixels are shown individually; in panel (c), the data were interpolated such that there is spatially continuous coverage.

is significant horizontal motion due to aquifer deformation. While there is some seasonal horizontal deformation due to groundwater withdrawals, the signal is primarily linear (i.e., elastic) and seasonal, while the vertical deformation is dominated by long-term, inelastic deformation signals (Smith et al., 2017; see also a nearby GPS station: https://www.unavco.org/instrumentation/networks/status/nota/overview/P056). Since the long-term deformation velocity is much higher magnitude than seasonal changes, and no seasonal data were used from this data set in the inversion, we consider this assumption to be appropriate.

3.3.3. Highway 198 Survey Point

The Highway 198 survey point provided a single measure of the total subsidence between "the 1960s" and 2004 as 1.7 m, as reported in Sneed et al. (2018). Considering that "the 1960s" could refer to anytime between 1960 and 1969, we converted 1.7 m into a range of deformation rates from 3.9 to 5.0 cm/yr, equivalent to 1.7 m over 44 or 34 years. The survey point is just north of our study area, as shown in Figure 2b. At the survey point, measurements from the two InSAR data sets record subsidence rates at 75% of the rates within our study area. To

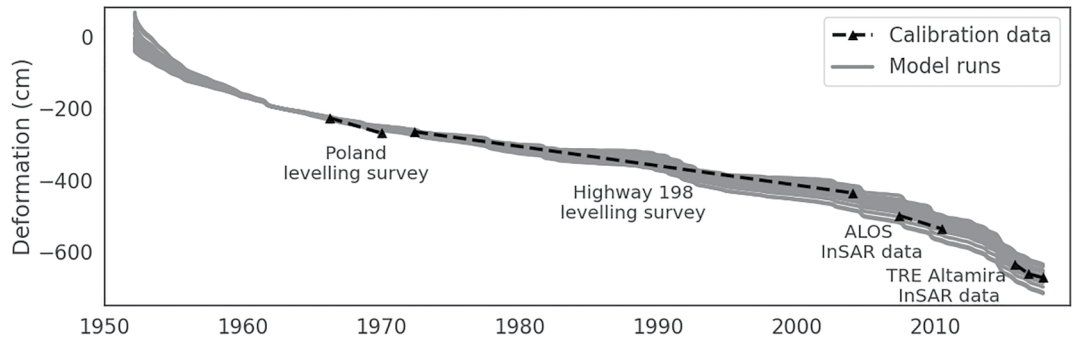

Figure 9. The 20 accepted simulations, plotted with the calibration data used. Over the period 1952–2017, we simulated over 6.5 m of subsidence at our study area.

account for the fact that our study area likely experienced slightly higher subsidence rates than the measurements at this survey point, we extended the bound slightly, and therefore applied the following acceptance criterion: the simulated subsidence between 1965 and 2004 was required to be between 90% and 160% of that recorded by the Highway 198 survey point; i.e., it had to have a mean rate over that period between 3.9 and 6.9 cm/yr. We do not have an estimate of the measurement error associated with the Highway 198 survey data. We assume that it will be significantly smaller than the uncertainty contained within our 3.9–6.9 cm/yr estimate.

3.3.4. Historic-Era Leveling Data

The historic-era survey data are a series of measurements made during the years 1933, 1947, 1953/4, 1957, 1958, 1962, 1966, and 1970 as reported in Poland et al. (1975) and the Inter-Agency Committee on Land Subsidence in the San Joaquin Valley (1958). They show low rates of subsidence until 1954, and high rates of subsidence from then until the end of the surveyed period in 1970. Since the early part of our simulations is strongly influenced by the initial conditions, we only used the 1966–1970 measurement for model calibration. The survey recorded an average subsidence rate of 11 cm/yr during those 4 years. However, the survey location is slightly south of our study area (see location in Figure 2b). At the survey location, measurements from the two InSAR data sets recorded subsidence rates 125% of the rates measured within our study area. To account for the fact that our study area likely experienced slightly lower subsidence rates than the measurements at this survey point, we extended this bound slightly, and applied the following acceptance criteria: the simulated subsidence rate between 1966 and 1970 was required to be between 65% and 100% of that recorded by the survey point; i.e., it had to have a mean rate over that period between 7 and 11 cm/yr. Formal estimates of measurement error from the historic-era leveling are not available, although Lofgren and Klausing (1969) suggested they can be expected to be accurate to tenths of a foot, which is significantly smaller than the uncertainty contained within our 3.9–6.9 cm/yr estimate.

3.3.5. Identification of Final Models

Our final models were those which matched all of the calibration data, within the ranges defined above. We did not favor those models with predicted subsidence rates nearer to the median of the ranges, since the ranges came from the spatial variation and we therefore consider them to be uniformly distributed. Once we identified the model simulations that matched the calibration data, we had the modeling results that provided the foundation for our study of the controls on subsidence: a multidecadal subsidence record in the three layers of our aquifer system. These were the models we then used to tackle our main research questions, which were to determine the depth intervals and time scales over which compaction occurs in our study area.

4. Results

Our final grid search involved 10,080 simulations producing subsidence time series from 1952 to 2017. Of those subsidence time series, only 20 were able to adequately fit the calibration data. These time series, and the calibration data, are shown in Figure 9.

The 20 accepted simulations mapped to a wide range of input parameters, and not to a small, specific region of the parameter space. We therefore concluded that the solution space was very nonunique, and that there were many

Table 3
The Input Parameters Used in the Grid Search, and the Values Which Were Accepted After the Calibration Process

Parameter	Input values	Accepted values
S_{skv}	$[6\times10^{-4}, 1.0\times10^{-3}, 1.8\times10^{-3}, 2.6\times10^{-3}, 3\times10^{-3}]$ m^{-1}	$[6\times10^{-4}, 1.0\times10^{-3}, 1.8\times10^{-3}, 2.6\times10^{-3}\times10^{-3}]$ m^{-1}
K_v	$[2.5\times10^{-7}, 5.0\times10^{-7}, 1.0\times10^{-6}, 1.5\times10^{-6}, 2.0\times10^{-6}, 2.5\times10^{-6}, 3.0\times10^{-6}]$ m day^{-1}	$[2.5\times10^{-7}, 5.0\times10^{-7}, 1.0\times10^{-6}, 1.5\times10^{-6}]$ m day^{-1}
$b_0(\Omega)$	$b_0(30.5)$, $b_0(33.0)$, $b_0(36.0)$, $b_0(39.0)$	$b_0(30.5)$, $b_0(33.0)$, $b_0(36.0)$, $b_0(39.0)$
$(h_0^{upper}, h_0^{lower})$	[(55, 39), (55, 49), (55, 54), (55, 60), (55, 65), (55, 71), (61, 39), (61, 49), (61, 54), (61, 60), (61, 65), (61, 71), (68, 39), (68, 49), (68, 54), (68, 60), (68, 65), (68, 71)] masl	[(55, 65), (55, 71), (61, 65) (61, 71), (68, 60), (68, 65), (68, 71)] masl
d_i	[50, 100, 150, 200] m	[50, 100, 150, 200] m
$\overline{\tau}$	487 discrete values between 6 and 2,585 years	[64, 86, 96, 144, 237, 258, 339, 517, 542, 700, 999, 1,008] years

Note. The notation $b_0(\Omega)$ in the third row means the distribution of clay thicknesses for a given ohm cutoff. Initial condition values are given as pairs of upper and lower heads.

trade-offs within the input parameters. The values of the input and accepted parameters are given in Table 3. Table 3 contains one derived parameter, which is the gross time scale $\overline{\tau}$. The accepted range of $\overline{\tau}$ reduced from 6–2,585 years in the input to 64–1,008 years in the accepted simulations.

In Figure 10 we present a display, from 1952 to 2017, of the head time series in the upper and lower aquifers (our input data) along with the simulated subsidence, now plotted as an annual rate to more clearly show the trends and the variation amongst our accepted simulations. Between the two plots, we show the times at which we had calibration data. Both the input head data, and the simulated subsidence, align with known hydrologic events. We see how known high levels of groundwater extraction in the 1940s, 1950s, and 1960s caused head to decline and subsidence to occur. Then, the high availability of surface water in the 1970s caused head to stabilize and, by the 1980s, recover, resulting in a reduction of subsidence rates. In the 1987–2017 period, four main dry/drought periods (1987–1992 drought, 2001–2004 dry period, 2007–2010 drought, and 2012–2015 drought) are clearly correlated with declining heads and spiking subsidence rates, with subsidence rates generally low between these events. Our simulated subsidence therefore fits within the wider hydrologic framework of events in the area. Notable is the observation that only in 1986 did we ever simulate a time period with no subsidence, when one of the 20 simulations saw uplift of 0.4 cm.

We can now examine how much compaction occurred in each of the three hydrostratigraphic layers (the upper aquifer, the lower aquifer, and the Corcoran Clay). This is shown for each water year in Figure 11. Overall, the majority (84%) of subsidence occurred due to compaction within the lower aquifer, with 12% occurring due to compaction in the upper aquifer and about 4% originating from the Corcoran Clay. However, these ratios did vary over time. The pie charts in Figure 11 emphasize this. The period 1952–1987 was when the thickness of the lower aquifer in the model was the smallest, and also a time when head was actively declining in the upper aquifer whereas it had already stabilized in the lower aquifer. In this time, about 78% of compaction occurred in the lower aquifer and 17% in the upper aquifer. Over time, the new, deeper pumping wells caused the base of the lower aquifer in our model to get deeper, and head changes contemporaneously became increasingly amplified in the lower aquifer. This resulted in the contribution to subsidence from the upper aquifer to reduce to 11% in the period 1987–1997 and 6% in the period 1997–2017. The contribution of the Corcoran Clay remained small, at 4–5%, in all three periods.

To explore the implications of the long gross time scales, we ran additional simulations with the aim of quantifying how much recent subsidence was due to past head changes. In these simulations, we fixed the head at its level from a past year and simulated the subsidence that would result, with no further changes in head, in 2017. We call these "abridged simulations". The results, shown in Figure 12, reveal that between 29% and 56% of the subsidence seen in 2017 was triggered by head drops prior to 2011, equivalent to a 2017 subsidence rate of ~5 cm/yr. These abridged simulations demonstrate that the long gross time scale creates high background levels of subsidence caused by the residual compaction of clays.

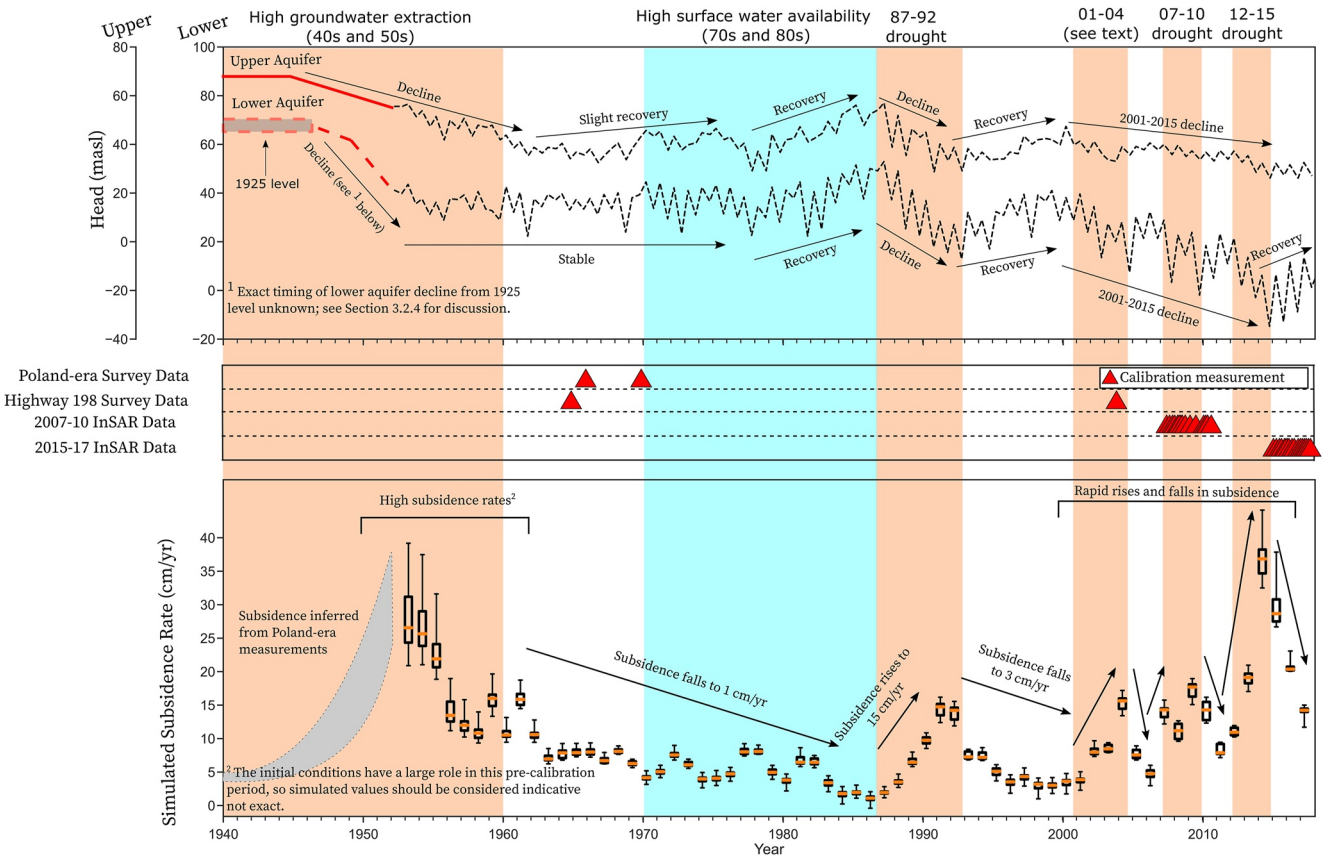

Figure 10. The relationship between hydrologic events, head, and simulated subsidence. Top: model input head time series, shown with the black dashed lines, for the upper and lower aquifers. Red lines pre-1952 show the approximated head trajectory prior to the model start date; for more information on this, see Section 3.2.4. Middle: observational subsidence data used in model calibration. Bottom: annual subsidence rates from the 20 simulations, shown as a box-and-whisker representation for each water year from 1952 to 2017. The whiskers represent the full range of simulated values, which the boxes show the interquartile range and the median simulated value for each year is represented with a horizontal orange line. Pre-1952 subsidence, shown in the gray arc, was inferred from Poland-era measurements reported in Poland et al. (1975) and the Inter-Agency Committee on Land Subsidence in the San Joaquin Valley (1958). Hydrologic events which caused the head variations are labeled at the top of the figure, and are marked with light orange (head decline) and cyan (head recovery) shading.

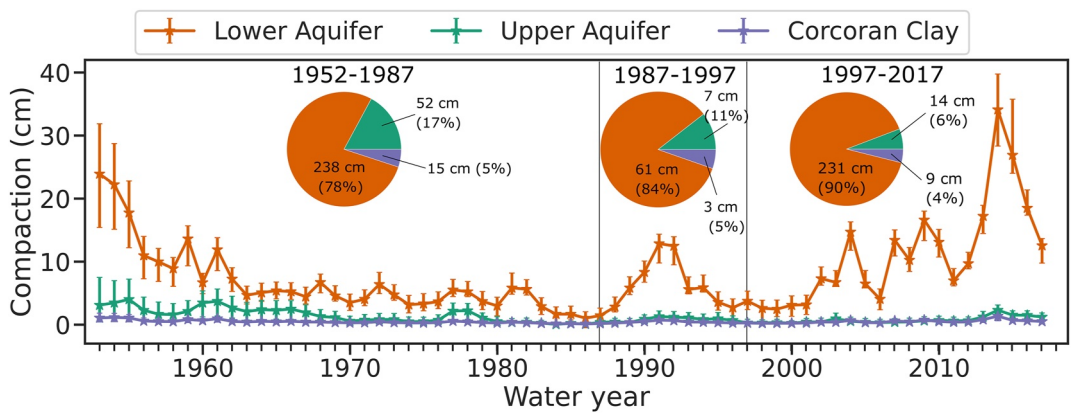

Figure 11. The partitioning of compaction between the upper aquifer, the lower aquifer, and the Corcoran Clay over time. Markers are the median simulated annual compaction values, with the error bars representing the range of simulated values. The three pie charts give the median simulated values for three time periods, and reveal how compaction in the upper aquifer has reduced in importance over time.

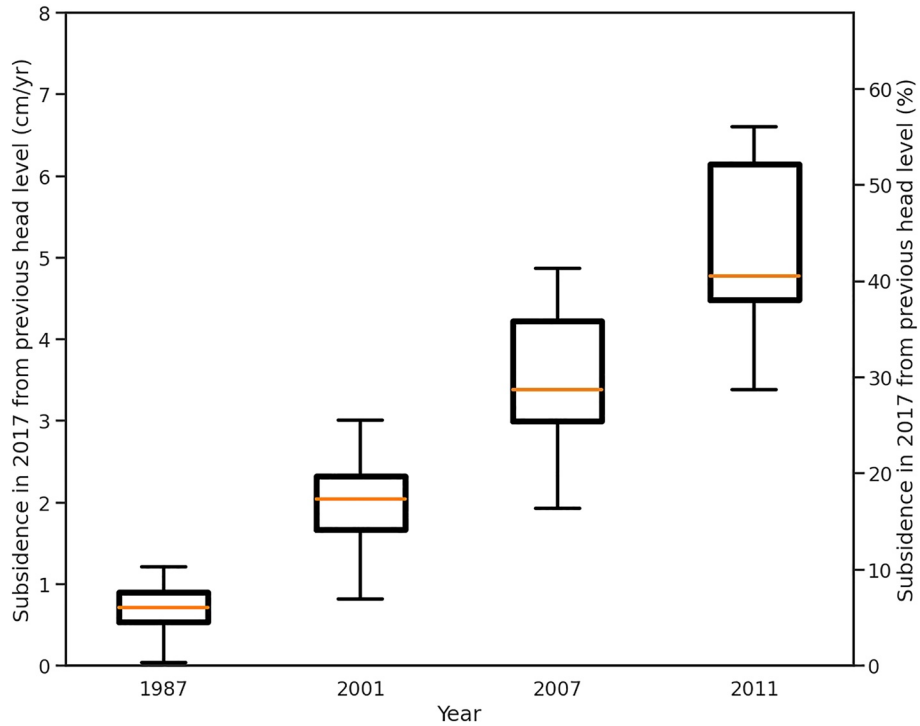

Figure 12. The results from the abridged simulations. For each of the 20 accepted simulations, we reran the model, but held head constant at its 1 January level in 1987, 2001, 2007, and 2011. Plotted are the 2017 subsidence rates in that circumstance, in units of cm/yr and the percent of the 2017 observed subsidence. The orange lines are the median of the 20 simulations, while the boxes show the 25 and 75th percentiles. The whiskers capture all 20 simulations.

5. Discussion

Our model makes insights which cannot be obtained from other subsidence models. 1D compaction models which take their hydraulic head inputs from groundwater flow models rely on an additional layer of assumptions about the fluxes into the groundwater system, in particular pumping and recharge, which are not routinely measured in the SJV; it is therefore valuable to perform 1D compaction models using measured head as input, as we have done here. Compared with Smith and Knight (2019), which also used measured head as input, our model covers a longer time period, allowing for a better treatment of the long time scales of residual compaction. Additionally, our model can partition compaction between the upper aquifer, Corcoran Clay, and lower aquifer, which theirs did not. Our model thus gives a unique way of dealing with subsidence.

One unique feature of our model was the use of four sets of calibration data, covering a range of time periods. Not surprisingly, we found that the more calibration data we used, the smaller the number of accepted simulations became. This suggests that using a greater amount of calibration data improves the resulting simulations. When using both sets of InSAR data, but no other calibration data, a larger group of 181 simulations were accepted. Conversely, when using only the Poland and Highway 198 calibration data, 601 simulations were accepted, and when using only the Poland calibration data, over 2,000 simulations were accepted. The suites of accepted simulations obtained when using different calibration data are shown in Figure 13. We conclude that calibrating with data from multiple time periods results in simulations with a substantially tighter range of outputs.

One objective of our modeling was to estimate the contribution to the total subsidence from the various depths over which compaction was occurring. It is interesting to compare our results with extensometer data at other locations in the Valley. To do this, we took data from the historic extensometer network (reported in Ireland et al. (1984)) and identified extensometers that were coincident with leveling surveys, since these could be used to estimate what portion of total subsidence came from compaction of the upper aquifer. Due to the small number of deep, multiscreened extensometers, this was possible at more locations than could be used to estimate lower aquifer compaction. There were four extensometers we could use, which are tabulated in Table S1 in Supporting

10.1029/2021WR031390

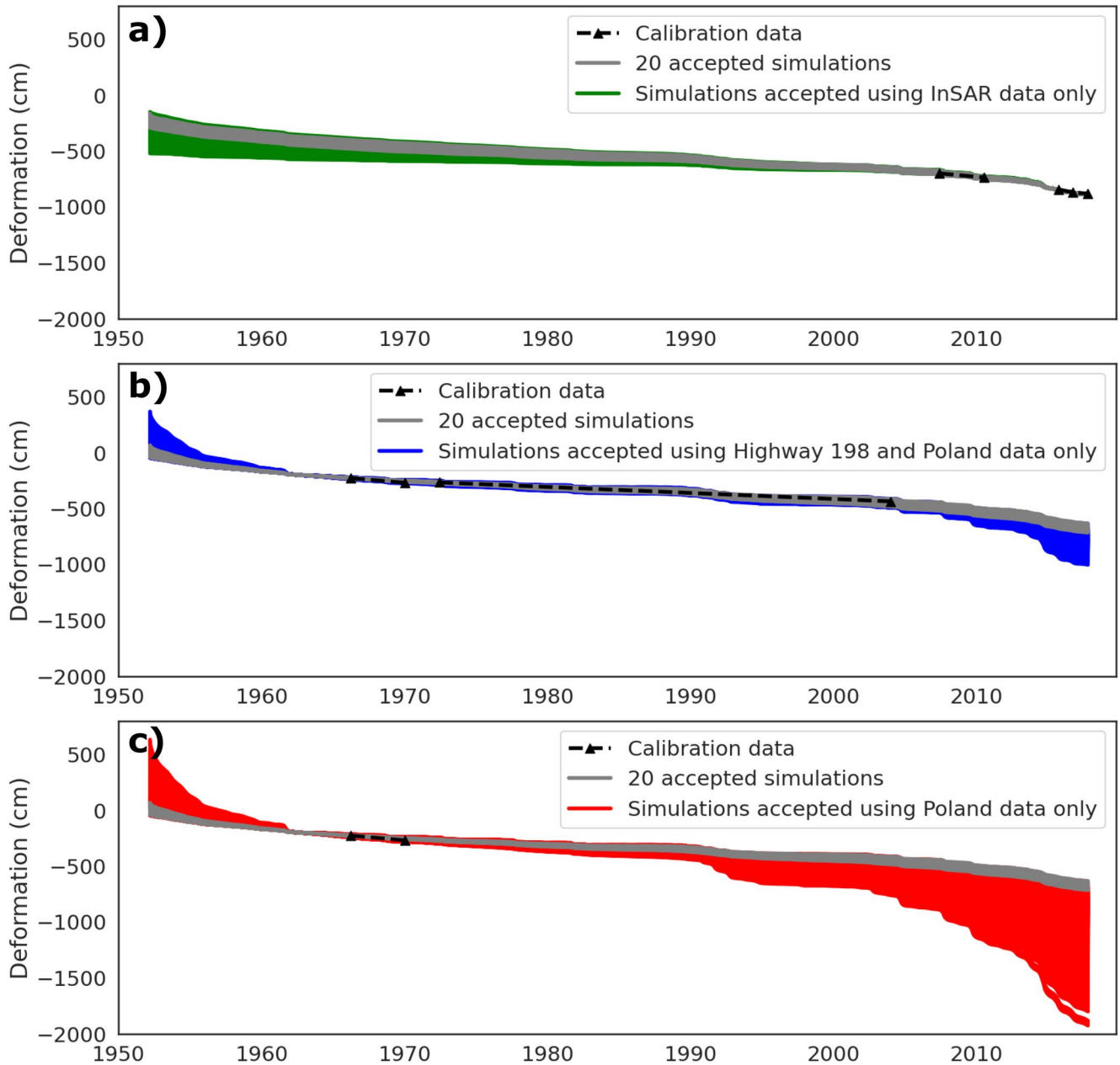

Figure 13. (a) The suite of 181 simulations obtained when calibrating with only the interferometric synthetic aperture radar (InSAR) data; (b) the suite of 601 simulations obtained when calibrating with only Poland and Highway 198 data; (c) the suite of 2,037 simulations obtained when calibrating with only the Poland data.

Information S1. They showed substantial variation in the amount of subsidence that originated as compaction in the upper aquifer, with values ranging from 2% to 43%. Our value of 17% for the 1952–1987 period is within this range. For a more recent comparison, only one extensometer can be used. That extensometer is the Fordel extensometer, which is coincident with a GPS station in the west of the Valley. Sneed et al. (2018) reported that 9% of subsidence between 2004 and 10 at the Fordel extensometer originated from the upper aquifer. Our value of 6% for the period 1997–2017 is slightly smaller, but broadly comparable to this value. It is worth noting that some discrepancy may be introduced by the fact we ignored the 25-m thick zone of the upper aquifer which drained over our modeled period. In general, our modeled values are comparable to those found extensometers elsewhere in the Valley, which gives us confidence in the validity of our findings.

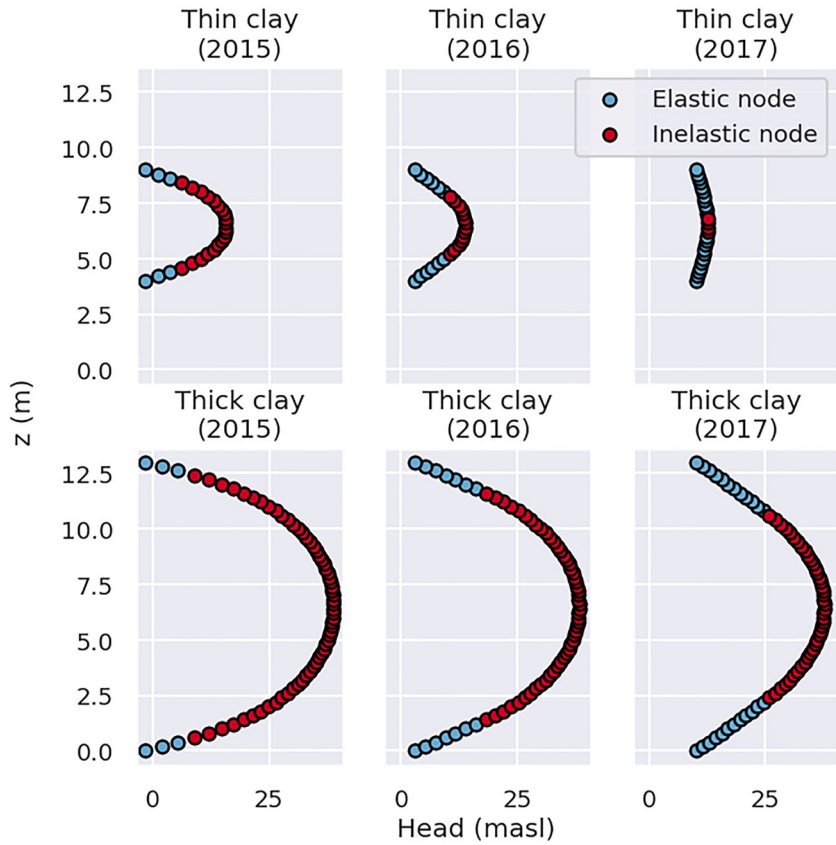

Figure 14. Illustration of the evolution of effective stress within a thin (top) and thick (bottom) clay during 2015, 2016, and 2017. In the thin clay, the clay goes from primarily inelastic to primarily elastic over the 3 years. The thick clay still retains a large region in its core which is compacting inelastically, even in 2017. This inelastic compaction of the core will continue for a long time, governed by $\tau_{inelastic}$, unless head recovery continues beyond 2017. The illustrated clays are interbeds from the lower aquifer of the simulation with the following parameters: b_0(33.0), S_{skv} = 1e−3 m^{-1}, K_v = 1.5e−6 m day^{-1}, d_i = 100 m, h_0^{upper} = 68 masl, h_0^{lower} = 65 masl.

Other studies have attempted to invert InSAR observations directly for the depth of compaction, using various hydrologic and other constraints, but without using the aquitard-drainage theoretical framework of compaction. Two such studies are Vasco et al. (2019) and Carlson et al. (2020), who inverted InSAR data to estimate compaction in at various depth intervals over the time periods 2015–2018 and 2007–2009, respectively. These studies have the advantage of being regional scale, but the theoretical basis for the inversion is less rigorous than our approach. Vasco et al. (2019) generally found the depth range 50–150 m (which corresponds most closely to the upper aquifer) to show the greatest compaction rates, a finding which was echoed in Carlson et al. (2020). This is different to the findings of our model. One explanation is that their models do not account for the head change in the upper aquifer being far less than that in the lower aquifer, which has been true in our study area since at least 1997. However, to fully explore the accuracy of the two approaches will require further work, as it is possible the differences are due to the local nature of our study.

Let us now focus on the issue of the time scale over which residual compaction of clays occurs. Our study could only fit the calibration data when $\overline{\tau}$ was between 64 and 1,008 years. These gross time scales are similar to those reported from early studies in the 1970s (Helm, 1978), and are also similar to the time scales seen for continued subsidence in the event of no further head drop in the recent study of Smith and Knight (2019). However, two recent papers which have looked at head and InSAR-derived subsidence, but have not modeled the drainage of clays, reported time scales for the residual compaction of clays of 0.5–1.5 years (Liu et al., 2019; Ojha et al., 2019). A third study, Smith et al. (2017), has been cited as reporting a 2 year time scale for residual compaction, but that study used the symbol τ to estimate that the thickness of sediments that would equilibrate

with aquifer heads in a 2-year period is roughly 36% of the total sediment thickness. In other words, their use of $\tau = 2$ years did not imply that no residual compaction would occur after 2 years.

We attribute the apparent discrepancy between the time scale of decades reported in our study and that of 0.5–1.5 years in two other studies to the presence of *two* subsidence time scales—one that is relevant in describing the elastic response of the system and one that is relevant in describing the inelastic response. As shown in Figure 14, the clay layers can exhibit a mixture of elastic and inelastic behavior; the determining factor is the magnitude of the effective stress relative to its historic maximum. If we consider the head recovery following the 2012–2015 drought, Figure 14 shows that the thinner clays and margins of the thicker clays experienced a reduction in effective stress during 2015–2017 in regions which were previously at their maximum effective stress. Therefore, this process was governed by the elastic time scale $\tau_{elastic}$, which has been estimated to range from 0.1 to 11 years (Ireland et al., 1984). Simultaneously, in the cores of the thicker clays, Figure 14 shows ongoing residual compaction, which is still governed by the inelastic time scale $\tau_{inelastic}$. In our study area, where subsidence was observed in 2017, the residual compaction outweighed the expansion, but both of these processes were occurring simultaneously. Based on our findings, we hypothesize that two subsidence time scales operate in the SJV, corresponding to elastic and inelastic processes within clays. When head levels stabilize at their historic minimum, subsidence will continue for the very long inelastic time scales (10s–100s of years). However, when head levels recover above that level, subsidence rates fall rapidly in accordance with the elastic time scale (∼1 year). We suspect that it is the latter time scale identified in the studies of Liu et al. (2019) and Ojha et al. (2019).

Given the recent passage of the SGMA legislation, it is important to consider our results in the context of groundwater management. We identify two major areas where our findings can be significant. First, our work shows that that the lower aquifer is responsible for the bulk of subsidence. This suggests the possible subsidence mitigation strategy of redirecting pumping from the lower aquifer to the upper aquifer. Further research into this possibility should be a priority. Our second relevant finding is that stabilizing head at or near its historic minimum levels does not cause subsidence to stop; subsidence could continue for 10s–100s of years in that situation due to continued residual compaction within thick clays. This is an important observation because analysis of SGMA plans within the Tulare Lake and Kaweah subbasins show that they all intend to reach sustainability by stabilizing head either at new lows or the 2015/2016 low (El Rico Groundwater Sustainability Agency et al., 2020; Petersen & Nicely, 2019; Provost & Prichard Consulting Group, 2020; Ricker et al., 2020). Based on our findings, in order to significantly reduce subsidence, there must be some recovery of head, not just a stabilization.

Although the aquitard-drainage conceptual framework of subsidence, on which our model is based, is our best current description of the physical mechanism by which subsidence arises, we now discuss four assumptions which could limit the accuracy of our modeling.

The first assumption made is that the coarser-grained sediments of both aquifers are perfectly interconnected, such that there is no vertical hydraulic head gradient within an aquifer. Although multiscreened observation wells do not exist in the SJV to assess this assumption, in the aquifers in the nearby Sacramento Valley, vertical head gradients are seen within aquifers. If this is also the case in the SJV, the likely impact is that the input heads we use for our modeling are a vertically averaged head across each aquifer. This is unlikely to significantly alter our conclusions regarding the time scales and depth intervals over which subsidence occurs. It does mean that our model should not be used to apportion compaction to smaller intervals within the two aquifers.

A second assumption is that the physical parameters are constant over time. In reality, S_{skv} values probably decline over time, since physical intuition as well as the laboratory insight presented in Helm (1975, 1976) suggests that, as compaction occurs, clay particles get closer to "ultimate compaction," and therefore deform less over time. Similarly, it is expected that K_v values might decline over time (Hoffmann et al., 2003b). This has implications for the magnitude of future subsidence, since it suggests that subsidence rates in the Valley may decrease, something our model does not account for. Intriguingly, if we select our simulations which only match the Poland leveling survey they tend to overpredict the subsidence observed by the ALOS and TRE Altamira InSAR, while those that only match the InSAR tend to underpredict the subsidence recorded by the Poland leveling survey (Figure 13). One explanation for this is decreasing S_{skv} values over time. However, the continued subsidence during the 2012–2015 drought indicates we are not yet at the stage where this is significantly reducing subsidence rates.

A third assumption is that all upper aquifer compaction occurs in the permanently saturated zone. This ignores 25 m of sediments which drained between 1952 and 2017, equivalent to about 35% of the compacting zone in the upper aquifer. Since we found that the total contribution of the upper aquifer was relatively small, we do not expect this assumption to have a significant impact on our conclusions; however, in another location, it could be significant.

A fourth assumption is that head measurements made over a small area are appropriate for a 1D model. The appropriateness of this assumption depends on the size of the area selected and the average horizontal head gradient. By choosing a small study area, we do not expect this assumption will have a large impact the validity of our results.

Although the small size of our study area allowed us to model subsidence at a high level of detail, it raises the obvious question of how representative are findings are of the broader SJV. Our results provide a framework for understanding the ways in which the magnitude and timing of subsidence is determined by the head time series and the presence of clay interbeds and confining layers, as well as the hydraulic and mechanical properties of the sediments in the aquifer system. This framework is true across the SJV. Since the general patterns observed in the head time series in our study area are similar, although not identical, to those seen Valley-wide (see, for instance, Chaussard & Farr, 2019), and the Corcoran Clay and a large number of clay interbeds are present in most subsiding locations, we expect our conclusions to be broadly representative. However, there are known locations where upper and lower aquifers head time series are markedly different to those at our study area, which could result in different partitioning of subsidence between the aquifer system layers. Additionally, there are subsiding locations where the Corcoran Clay is not present, which correspond to a different hydrogeologic structural framework for modeling subsidence. Finally, the heterogeneity of the aquifer system may lead to differences in the thicknesses and hydraulic and mechanical properties of clays, which would alter time scales over which compaction occurs. Sneed (2001) showed little spatial variation in the mechanical properties of clays, but additional work needs to be done before it can be concluded that hydraulic properties and thicknesses are similar Valley-wide. We therefore believe that our conclusions may provide insights into the controls on subsidence throughout the Valley, while acknowledging that detailed modeling studies at other locations will be required to confirm this.

6. Conclusion

At time of writing (October 2021), the SJV is again in a state of extreme drought, with its two constituent parts—the Tulare Basin and the San Joaquin Basin—having recorded their first and third driest years on record (California Data Exchange Center, 2021). With the enactment of the SGMA legislation, the damaging impacts of land subsidence caused from groundwater overdraft were codified in law for the first time. Today, the key challenge faced in the Valley is managing groundwater sustainably given the vast agricultural industry, the increasingly large urban population, and the needs of groundwater dependent ecosystems.

The modeling presented in this paper provides a way to obtain new information on the time scales and depth intervals over which subsidence occurs. It is a way to reinforce what we already know from previous modeling, observations and data analysis, as well as providing new insights. Of particular significance is the warning that subsidence will continue, not for one-to-two years, but for multiple decades, if hydraulic head levels do not recover. We also find some good news: if head *does* recover, the reduction in subsidence occurs over short periods, of one-to-two years, due to elastic deformation within clays. Insights such as these will be critical for the SJV to tackle subsidence, and increasingly so following the past year of extreme drought.

Appendix A: Derivation of Governing Time Scale

First, define the following nondimensional variables:

$$\hat{t} = \frac{t}{\tau_{general}} \tag{A1}$$

$$\hat{z} = \frac{z}{b_0} \tag{A2}$$

$$\hat{\sigma'} = \frac{\sigma'}{\overline{\sigma'}} \tag{A3}$$

where $\tau_{general}$ is the general governing time scale (to be solved for), b_0 is the domain size over which Equation 1 applies and $\overline{\sigma'}$ is a typical value for effective stress.

If we substitute Equations A1–A3 into Equation 1, we get

$$\frac{K_v}{S_s b_0^2} \frac{\partial^2 \overline{\sigma'}}{\partial \hat{z}^2} = \frac{1}{\tau_{general}} \frac{\partial \overline{\sigma'}}{\partial \hat{t}} \tag{A4}$$

From which dimensional analysis shows us that

$$\tau_{general} \propto \frac{b_0^2 S_s}{K_v} \tag{A5}$$

We can see that $\tau_{general} \propto \tau$, where τ is the time constant defined in Equation 4.

Glossary

Effective stress (σ'): The grain-to-grain stress experienced within a sediment, related to head (h) and overburden stress (σ) by $\sigma' = \sigma - \rho g h$.

Overburden stress (σ): The stress acting due to the weight of overlying sediments and water.

Interbed: A clay layer embedded within an aquifer.

Confining layer: A clay layer which separates two aquifers.

Inelastic time constant: Characteristic time constant of compaction, derived assuming constant initial head and a step-change in boundary condition, for a clay layer experiencing its historic maximum of stress.

Elastic time constant: Characteristic time constant of compaction, derived assuming constant initial head and a step-change in boundary condition, for a clay layer not experiencing its historic maximum of stress.

Gross time constant: An aggregate time constant, representing the approximate time over which residual compaction of clays will occur in an aquifer system.

Data Availability Statement

The model code is archived at Lees (2022b). The simulations and raw input data used to derive the model inputs have been archived at Lees (2022a). Some of the data are not publicly available, so are "hidden" in the repository. These data may be available on request to the author if they are needed to validate or verify this study. The ALOS InSAR data used in this study were from a previous study (Smith & Knight, 2019) and the 2015–2017 data can be found from the California Department of Water Resources. Maps were made using the Python wrapper for the Generic Mapping Tools, known as PyGMT (Uieda et al., 2021; Wessel et al., 2019).

Acknowledgments
We would like to thank Dennis Mills (Kings County Water District) for providing the continuously monitored head data at Well H, and Larry Dotson (Kaweah Delta Water Conservation District) for providing the borehole data sets. We thank Tim Nicely, Eric Osterling, and Larry Dotson for providing the local head data set. This work was funded by the Gordon and Betty Moore Foundation (Grant GBMF6189) and by the NASA Applied Sciences Water Resources Program in the Earth Science Division (Grant 80NSSC19K12480), with M. Lees supported by a Stanford Graduate Fellowship.

References

Borchers, J., & Carpenter, M. (2014). *Land subsidence from groundwater use in California*. California Water Foundation. Retrieved from https://cawaterlibrary.net/wp-content/uploads/2017/04/1397858208-SUBSIDENCEFULLREPORT_FINAL.pdf

Brewster, B., Alacron, J., Hull, R., McKenzie, C., Nordberg, M., & Tung, J. (2015). *California's groundwater update 2013—Appendix "E" calculating annual change in groundwater storage using groundwater level data contents* (pp. 1–23).

California Data Exchange Center.(2021). Retrieved from https://cdec.water.ca.gov/index.html

California Department of Water Resources. (2021). *Periodic groundwater level measurements*. Retrieved from https://data.cnra.ca.gov/dataset/periodic-groundwater-level-measurements

Carlson, G., Shirzaei, M., Ojha, C., & Werth, S. (2020). Subsidence-derived volumetric strain models for mapping extensional fissures and constraining rock mechanical properties in the San Joaquin Valley, California. *Journal of Geophysical Research: Solid Earth*, *125*, e2020JB019980. https://doi.org/10.1029/2020JB019980

Chaussard, E., & Farr, T. G. (2019). A new method for isolating elastic from inelastic deformation in aquifer systems: Application to the San Joaquin Valley, CA. *Geophysical Research Letters*, *46*, 10800–10809. https://doi.org/10.1029/2019GL084418

Chen, J., Zebker, H. A., & Knight, R. (2015). A persistent scatterer interpolation for retrieving accurate ground deformation over InSAR-decorrelated agricultural fields. *Geophysical Research Letters*, *42*, 9294–9301. https://doi.org/10.1002/2015GL065031

Corbett, F., Schetrit, T., & Harter, T. (2011). *Crop water use, groundwater flow, and subsidence at Naval Air Station Lemoore, Fresno and Kings County, California*. (p. 353).Retrieved from https://ucanr.edu/sites/groundwater/files/151203.pdf

Farr, T. G., Jones, C., & Zhen, L. (2015). *Progress report: Subsidence in the Central Valley, California*. Retrieved from https://data.cnra.ca.gov/dataset/nasa-jpl-insar-subsidence/resource/17ad6fd5-918b-4cb2-b682-940ed1c8deb2

Farr, T. G., & Liu, Z. (2014). Monitoring subsidence associated with groundwater dynamics in the Central Valley of California using interferometric radar. *Remote sensing of the terrestrial water cycle*, 397–406. https://doi.org/10.1002/9781118872086.ch24

Faunt, C. (2009). Groundwater availability of the Central Valley aquifer, California introduction, overview of hydrogeology, and textural model of California's Central Valley (U.S. Geological Survey Professional Paper No. 1766. (p. 225). Retrieved from https://pubs.usgs.gov/pp/1766/

Faunt, C., Sneed, M., Traum, J., & Brandt, J. T. (2016). Water availability and land subsidence in the Central Valley, California, USA. *Hydrogeology Journal*, *24*(3), 675–684. https://doi.org/10.1007/s10040-015-1339-x

Gordon, G. V., & Croft, M. G. (1964). *Data for wells and streams in the Hanford-Visalia area, San Joaquin Valley, California (USGS Open File Report*. (p. 432). U.S. Department of the Interior, Geological Survey, Water Resources Division. Retrieved from https://searchworks.stanford.edu/view/13875451

Harding, S. T. (1927). *Ground water resources of the Southern San Joaquin Valley (Bulletin No. 11*). (p. 164). State of California Department of Public Works. Retrieved from https://archive.org/details/ssanjoaquingrou00hardrich

Helm, D. C. (1974). *Evaluation of stress-dependent aquitard parameters by simulating observed compaction from known stress history*. University of California.

Helm, D. C. (1975). One-dimensional simulation of aquifer system compaction near Pixley, California: 1. Constant parameters. *Water Resources Research*, *11*(3), 465–478. https://doi.org/10.1029/WR011i003p00465

Helm, D. C. (1976). One-dimensional simulation of aquifer system compaction near Pixley, California: 2. Stress-dependent parameters. *Water Resources Research*, *12*(3), 375–391. https://doi.org/10.1029/WR012i003p00375

Helm, D. C. (1977). Estimating parameters of compacting fine-grained interbeds within a confined aquifer system by a one-dimensional simulation of field observations. *Proceedings of the Anaheim Symposium, 121* (p. 12l).International Association of Hydrological Sciences.

Helm, D. C. (1978). Field verification of a one-dimensional mathematical model for transient compaction and expansion of a confined aquifer system. *Presented at the verification of mathematical and physical models in hydraulic engineering* (pp. 189–196). ASCE. Retrieved from https://cedb.asce.org/CEDBsearch/record.jsp?dockey=0027836

Hoffmann, J., Galloway, D., & Zebker, H. A. (2003). Inverse modeling of interbed storage parameters using land subsidence observations, Antelope Valley, California. *Water Resources Research*, *39*(2), 1031. https://doi.org/10.1029/2001WR001252

Hoffmann, J., Leake, S., Galloway, D., & Wilson, A. (2003). *MODFLOW-2000 ground-water model—User guide to the subsidence and aquifer-system compaction (SUB) Package (Open-File Report*). Retrieved from https://pubs.usgs.gov/of/2003/ofr03-233/

Holzer, T. (1998). The history of the aquitard-drainage model. Land subsidence case studies and current research. *Proceedings of the Dr. Joseph F. Poland Symposium on Land Subsidence*, 7–12.

Hung, W.-C., Hwang, C., Liou, J.-C., Lin, Y.-S., & Yang, H.-L. (2012). Modeling aquifer-system compaction and predicting land subsidence in central Taiwan. *Engineering Geology*, *147–148*, 78–90. https://doi.org/10.1016/j.enggeo.2012.07.018

Inter-Agency Committee on Land Subsidence in the San Joaquin Valley. (1958). *Progress report: Land-Subsidence Investigations San Joaquin Valley, California through 1957*.

Ireland, R. L., Poland, J. F., & Riley, F. S. (1984). *Land subsidence in the San Joaquin Valley, California, as of 1980 (USGS numbered Series No. 82-370)*. U.S. Geological Survey. Retrieved from http://pubs.er.usgs.gov/publication/ofr82370

Jeanne, P., Farr, T. G., Rutqvist, J., & Vasco, D. W. (2019). Role of agricultural activity on land subsidence in the San Joaquin Valley, California. *Journal of Hydrology*, *569*, 462–469. https://doi.org/10.1016/j.jhydrol.2018.11.077

Lees, M. (2022a). Data repository for development and application of a 1D compaction model to understand 65 years of subsidence in the San Joaquin Valley. Retrieved from https://purl.stanford.edu/vk278sy7516

Lees, M. (2022b). Retrieved from https://doi.org/10.5281/zenodo.6081094. *Zenodo*

Levy, M. C., Neely, W. R., Borsa, A. A., & Burney, J. A. (2020). Fine-scale spatiotemporal variation in subsidence across California's San Joaquin Valley explained by groundwater demand. *Environmental Research Letters*, *15*(10), 104083. https://doi.org/10.1088/1748-9326/abb55c

Liu, Y., & Helm, D. C. (2008). Inverse procedure for calibrating parameters that control land subsidence caused by subsurface fluid withdrawal: 1. Methods. *Water Resources Research*, *44*, W07423. https://doi.org/10.1029/2007WR006605

Liu, Z., Liu, P.-W., Massoud, E., Farr, T. G., Lundgren, P., & Famiglietti, J. S. (2019). Monitoring groundwater change in California's Central Valley using Sentinel-1 and GRACE observations. *Geosciences*, *9*(10), 436. https://doi.org/10.3390/geosciences9100436

Lofgren, B. E., & Klausing, R. L. (1969). *Land subsidence due to ground-water withdrawal Tulare-Wasco area California* (Professional Paper).

Mendenhall, W. C., Dole, R. B., & Stabler, H. (1916). Ground water in San Joaquin Valley, California (Water Supply Paper No. 398). *Water Supply Paper*. USGS. https://doi.org/10.3133/wsp398

Murray, K. D., & Lohman, R. B. (2018). Short-lived pause in Central California subsidence after heavy winter precipitation of 2017. *Science Advances*, *4*(8), 1–9. https://doi.org/10.1126/sciadv.aar8144

Neely, W. R., Borsa, A. A., Burney, J. A., Levy, M. C., Silverii, F., & Sneed, M. (2021). Characterization of groundwater recharge and flow in California's San Joaquin Valley from InSAR-observed surface deformation. *Water Resources Research*, *57*, e2020WR028451. https://doi.org/10.1029/2020WR028451

Ojha, C., Farr, T. G., Werth, S., Shirzaei, M., & Argus, D. F. (2018). Sustained groundwater loss in California's Central Valley exacerbated by intense drought periods. *Water Resources Research*, *54*, 4449–4460. https://doi.org/10.1029/2017WR022250

Ojha, C., Werth, S., & Shirzaei, M. (2019). Groundwater loss and aquifer system compaction in San Joaquin Valley during 2012–2015 drought. *Journal of Geophysical Research: Solid Earth*, *124*, 3127–3143. https://doi.org/10.1029/2018JB016083

Petersen, C., & Nicely, T. (2019). *Groundwater sustainability plan: Mid-Kaweah groundwater sustainability agency*. Retrieved from https://1e9875cc-fed9-417a-a220-06688759d310.filesusr.com/ugd/55be79_0dd4bb3a882641efa526ccc63e4c07a0.pdf

Poland, J. F., Lofgren, B. E., Ireland, R. L., & Pugh, R. G. (1975). *Land subsidence in the San Joaquin Valley, California, as of 1972 (U.S. Geological Survey Professional Paper No. 437-H)*. (p. 87). USGS.

Provost & Prichard Consulting Group. (2020). *East Kaweah GSA groundwater sustainability plan*. Retrieved from https://cawaterlibrary.net/document/east-kaweah-gsa-groundwater-sustainability-plan/

Ricker, M., Fricke, R., & Nicely, T. (2020). *Groundwater sustainability plan: Greater Kaweah groundwater sustainability agency*. Retrieved from https://greaterkaweahgsa.org/resources/groundwater-sustainability-plan/

Smith, R., Hashemi, H., Chen, J., & Knight, R. (2021). Apportioning deformation among depth intervals in an aquifer system using InSAR and head data. *Hydrogeology Journal*, *29*, 2475–2486. https://doi.org/10.1007/s10040-021-02386-0

Smith, R., & Knight, R. (2019). Modeling land subsidence using InSAR and airborne electromagnetic data. *Water Resources Research*, *55*, 2801–2819. https://doi.org/10.1029/2018WR024185

Smith, R., Knight, R., Chen, J., Reeves, J. A., Zebker, H. A., Farr, T. G., & Liu, Z. (2017). Estimating the permanent loss of groundwater storage in the Southern San Joaquin Valley, California. *Water Resources Research*, *53*, 5998–6017. https://doi.org/10.1002/2016WR019804

Smith, R., Knight, R., & Fendorf, S. (2018). Overpumping leads to California groundwater arsenic threat. *Nature Communications*, *9*(1), 1–6. https://doi.org/10.1038/s41467-018-04475-3

Sneed, M. (2001). *Hydraulic and mechanical properties affecting ground-water flow and aquifer system compaction, San Joaquin Valley, California (USGS Open-File Report No. 01-35* (p. 32).Retrieved from https://pubs.er.usgs.gov/publication/ofr0135

Sneed, M., Brandt, J. T., & Solt, M. (2018). *Land subsidence along the California aqueduct in West-Central San Joaquin Valley, California, 2003–10 (USGS Scientific Investigations Report No. 5144)*. Retrieved from https://pubs.er.usgs.gov/publication/sir20185144

Swanson, A. (1998). Land subsidence in the San Joaquin Valley, updated to 1995. *Land subsidence case studies and current research. Proceedings of the Dr. Joseph F. Poland Symposium on Land Subsidence*, 75–79.

Towill, Inc. (2021). *InSAR data accuracy for California Groundwater Basins CGPS data comparative analysis January 2015 to October 2020*. Retrieved from https://data.cnra.ca.gov/dataset/tre-altamira-insar-subsidence/resource/a1949b59-2435-4e5d-bb29-7a8d432454f5

TRE ALTAMIRA Inc. (2020*). InSAR land surveying and mapping services in support of the DWR SGMA program—Technical Rep*ort. Retrieved from https://data.cnra.ca.gov/dataset/tre-altamira-insar-subsidence/resource/2535a9b9-ed25-4b19-9734-4b1409e3fdce

Tulare Lake subbasin groundwater sustainability plan. Retrieved from https://cawaterlibrary.net/document/tulare-lake-subbasin-groundwater-sustainability-plan/

Uieda, L., Tian, D., Leong, W. J., Schlitzer, W., Toney, L., Grund, M., et al. (2021). PyGMT: A Python interface for the generic mapping tools. *Zenodo*. https://doi.org/10.5281/zenodo.5162003

Vasco, D. W., Farr, T. G., Jeanne, P., Doughty, C., & Nico, P. (2019). Satellite-based monitoring of groundwater depletion in California's Central Valley. *Scientific Reports*, *9*(1), 1–14. https://doi.org/10.1038/s41598-019-52371-7

Wessel, P., Luis, J. F., Uieda, L., Scharroo, R., Wobbe, F., Smith, W. H. F., & Tian, D. (2019). The generic mapping tools Version 6. *Geochemistry, Geophysics, Geosystems*, *20*, 5556–5564. https://doi.org/10.1029/2019GC008515

Williamson, A. K., Prudic, D. E., & Swain, L. A. (1989). *Ground-water flow in the Central Valley. California (USGS Professional Paper No. 1401-D*, p. 136). Retrieved from https://pubs.er.usgs.gov/publication/pp1401D